1

Theory of Plasmonic Excitations

Fundamentals and Applications in Photocatalysis

Lucas V. Besteiro[1,2], Xiang-Tian Kong[1], Zhiming M. Wang[1] and Alexander O. Govorov[1,3]

[1] *Institute of Fundamental and Frontier Sciences, University of Electronic Science and Technology of China, Chengdu, China*
[2] *Institut National de la Recherche Scientifique, Centre Énergie, Matériaux et Télécommunications, Varennes, QC, Canada*
[3] *Department of Physics and Astronomy, Ohio University, Athens, OH, USA*

1.1 Introduction

Plasmonic systems have become a common tool in a variety of subfields of nanotechnology, be it to manipulate the propagation of light or to harvest its energy. The fundamental properties that make them attractive and versatile are their large interaction cross-sections and a great degree of spectral tunability, both arising from the resonant nature of their interaction with light [1]. We can therefore use them as nanoantennas capable of effectively controlling the flow of light at frequencies ranging from the ultraviolet (UV) to the infrared (IR). Although, historically, a good amount of interest in plasmonics was directed toward creating optical metamaterials [2, 3], the fundamentally lossy nature of plasmonic materials, such as noble metals, introduced practical limits on their use in optical devices [4]. This invited many researchers to find ways for taking advantage of the nonradiative losses of plasmonic systems [5, 6]. Some examples include their usage as photoheaters [7–10], photodetectors [6, 11–13], or, most relevantly to the contents of this book, as photosensitizing elements in photocatalysis and photoelectrochemistry [14–22]. In order to understand why plasmonic nanoparticles (NPs) are of interest in the context of chemical catalysis, we should explore the fundamental properties of metallic materials, and how these impact their interaction with light and with their environment, so that they can drive chemical reactions. In this chapter, we will discuss the above points, providing a general theoretical perspective of the dynamics of plasmonic excitation in NPs, and the mechanisms by which energy can be transferred from a coherent plasmonic oscillation to the environment.

Before commencing a detailed description of the internal dynamics in plasmonic systems, it would be convenient to contrast the fundamental properties of these materials with those of semiconductors, more conventional heterogeneous photocatalysts [24]. In doing so, we will highlight the relevance of electronic structure

Plasmonic Catalysis: From Fundamentals to Applications, First Edition.
Edited by Pedro H.C. Camargo and Emiliano Cortés.

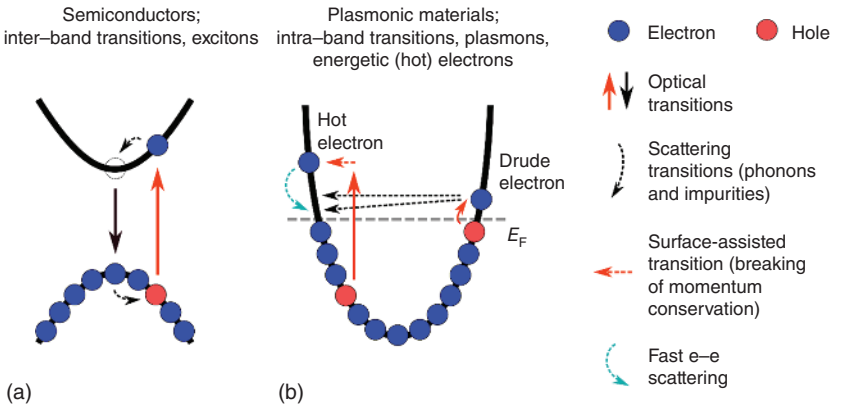

Figure 1.1 Schematic representation of the typical electronic states in two relevant types of materials used in heterogeneous photocatalysis: (a) semiconductors and (b) plasmonic crystals. The diagrams include the main optical excitation channels connecting the electronic states in these materials, as well as characteristic relaxation mechanisms. Plasmonic crystals are conductive and can be metals, degenerately doped semiconductors, or conducting oxides. *Source*: Adapted with permission from Ref. [23] Copyright 2019 Elsevier.

in determining the optical properties of a given material. Semiconductors are crystalline solids, and the periodicity of their structure gives rise to bands with a continuum of electronic states. These bands are key quantum properties of the periodic lattice of a crystal, and contrast with the discrete electronic states in atoms and molecules. A schematic representation of this can be seen in Figure 1.1a, which depicts the electronic structure of a typical bulk semiconductor, showcasing also its characteristic bandgap separating occupied and unoccupied states. Optical transitions can excite electrons across the bandgap, generating relatively long-lived electron–hole pairs that can drive surface chemistry in photocatalytic systems, targeting different redox reactions depending on their relative energy alignment with the valence or conduction band of the semiconductor. They are widely used in photoelectrochemical cells [25, 26] and other photocatalytic setups [27, 28], employing both bulk and nanostructured semiconductor materials as a repository of optically excited charge carriers for driving the target reaction. These long-lived carriers can be extracted via contacts since semiconductors, when doped, possess high conductivities and are suitable for building electrochemical circuits [25, 29]. At the same time, the bandgap introduces a threshold on the energy of the photons that can be absorbed, which limits the fraction of the solar spectrum available for conversion. This shortcoming of semiconductors as photocatalysts under solar irradiation has been one of the motivations for combining them with plasmonic systems [15].

Plasmonic materials are also crystalline solids, but their defining characteristic is their large number of mobile carriers. The paradigmatic case for this is a metal, whose electronic bands overlap in energy across the reciprocal space and therefore lacks a bandgap, although materials like conductive oxides and highly doped semiconductors can also support plasmonic resonances [30–32]. Direct optical transitions such as those occurring in semiconductors are not possible within a

metal conduction band, due to conservation of momentum, unless it is allowed through quantum confinement in the system or the interaction of the electron with crystal defects or phonons [33, 34]. This is sketched in Figure 1.1b, but we will discuss it in more detail when describing the excitation of hot electrons (HEs) and hot holes (HHs). On the contrary, the distinctive mode of interaction of plasmonic systems with light occurs through the collective excitation of the electrons in the system. The electrons in the conduction band oscillate coherently, with small changes in energy and momentum for each of them, collectively constituting the excitation of the plasmonic particle.

It is illustrative to consider such a particle in a fully classical way, where the cloud of free electrons moves in a continuous manner following an external electric field. If the frequency of the driving field is slow enough, the mobile charges in the conductive particle remain in phase with the external field and equilibrium between field and internal polarization is maintained, resembling a typical electrostatic picture (Figure 1.2a). As we consider higher frequencies, however, we will approach the natural or intrinsic resonance of the particle. This resonant frequency will depend on the number and mobility of the carriers in the conduction band, as well as the geometry of the particle. When the external field excites the system at its resonant frequency, the charge oscillation in the particle will lag behind the external field by a phase of $\pi/2$, resulting in an internal polarization that does not cancel out the driving field, but is instead amplified by it (Figure 1.2b). This is of course analogous to the behavior of classical mechanical oscillators when driven resonantly at their natural frequency [36]. Likewise, a plasmonic NP excited at its plasmonic resonance will increase the amplitude of its oscillation, i.e. will show a larger charge polarization, giving rise to the well-known plasmonic enhancement of the particle's near field. It will also continue oscillating if the driving force is stopped, to then reduce its amplitude as the oscillation is dampened or, in a complementary perspective, the plasmon decays. Understanding how different mechanisms contribute to dissipating the energy in the plasmon will be crucial to discuss how plasmonic systems can contribute to photocatalysis, so we will describe them separately in different sections of this chapter.

This resonant excitation of a large number of carriers in the conduction band is responsible for the large interaction cross-sections of plasmonic NPs, much larger than those of semiconductor QDs. This difference can reach several orders of magnitude, as exemplified by the data in Figure 1.2c. Furthermore, and because the movement of electrons will be constrained by the size and shape of the particle, the collective excitation of the mobile carriers also provides metal NPs with a strong spectral tunability of their plasmonic resonances. Using a given conductive material, we can determine the resonant frequency of a nanocrystal (NC) by considering different geometries. The shape and size of the NC sets the physical extension of the effective electromagnetic resonator composed by the electrons moving freely within the metal. Figure 1.2c,d illustrate this by showing the large shift between the plasmonic resonance of an Au spherical NP and an Au nanorod (NR). Importantly, it is not just the aspect ratio of the structure that determines its resonant frequency, but its curvature is critical as well. In Figure 1.2d, we see how the spectrum of an Au cube differs significantly than that of a sphere with the same volume. The curvature

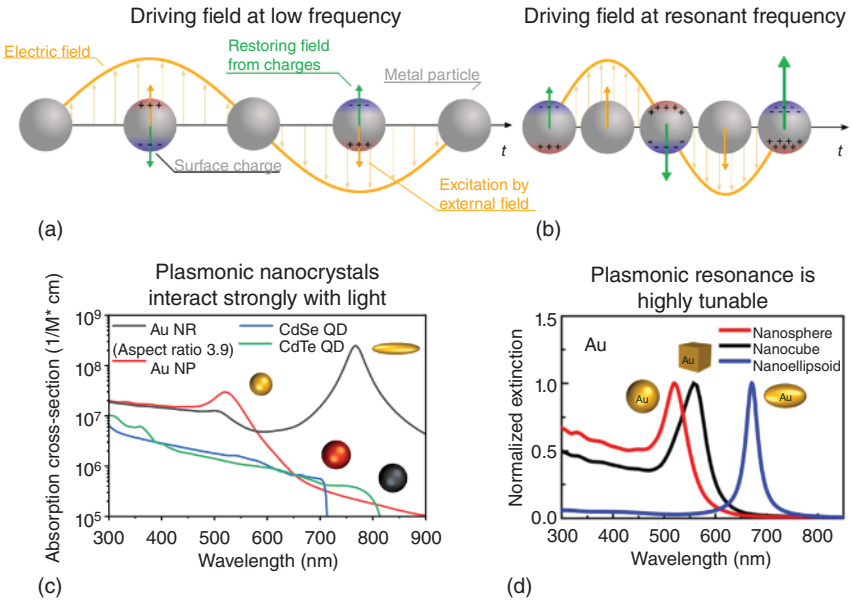

Figure 1.2 (a) Schematic diagram of metal nanoparticles driven at a low frequency. The electrons in the conduction band can follow the fields, with the resulting polarization field being in opposition to the driving field. (b) Same system under a higher frequency external field, exciting the plasmonic resonance of the particles. In this case the polarization field lags behind the driving field, is amplified by the driving field, and creates an enhanced near field around the particle. (c) Calculated absorption cross-sections of NCs made of different materials, but preserving the same volume. Plasmonic NCs absolutely dominate in terms of light–matter interaction strength. (d) Extinction cross-sections for gold particles with different shapes. By using different NC geometries, we can tailor the response of a given material. *Source*: Adapted with permission from Refs. (c) [33] Copyright 2019 American Chemical Society, (d) [35] Copyright 2014 Elsevier.

of the surfaces will also impact the distribution of the enhanced electric field around the particle. Combining their large cross-sections and their tunability, we can design plasmonic systems that can strongly interact with light across the full spectrum of solar radiation. In this way we can capture a large proportion of the incoming light flux with relatively low particle concentrations.

It should also be noted, however, that real metals also exhibit single-electron optical excitations. Electrons in fully occupied bands below the Fermi energy can be promoted to higher-energy empty states through direct optical transitions if the photon energy is sufficiently large. Such a promotion is referred to as an interband transition, and contrasts with the intraband transitions that occur within the semi-occupied conduction band. We include a schematic illustration of interband transitions in Figure 1.3a, taking Au as an example material. Optical transitions of this type are commonplace in real materials and are responsible for their response in the short wavelength part of the spectrum. Interband transitions are the reason why the spectra of Au NCs in Figure 1.2c,d are not a simple plasmonic resonance and show instead a significant absorption profile at wavelengths below ~540 nm.

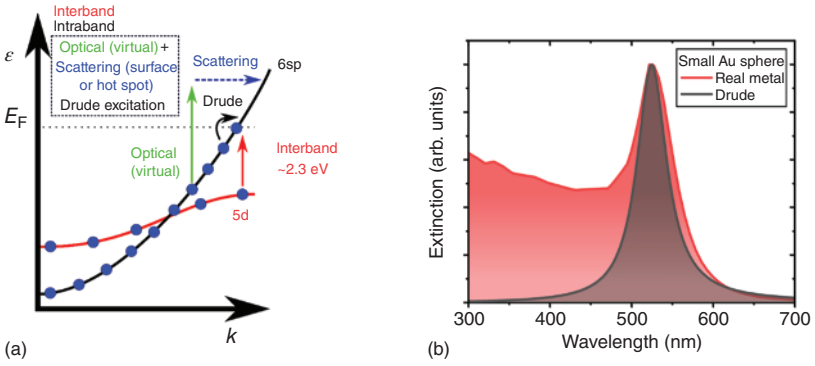

Figure 1.3 (a) Schematic diagram of the band structure of gold, depicting the conducting band and the fully occupied *d* band. We also note relevant optically-induced electronic transitions. (b) Extinction of a small Au sphere in water, calculated under the quasistatic approximation. We contrast results obtained with experimental bulk permittivity data from gold (red) and from the Drude model (black). The Drude data only models the carriers in the conduction band, and does not include interband transitions. *Source*: Panel (a) was adapted with permission from Ref. [23] Copyright 2019 Elsevier.

These interband processes are single-electron transitions, they scale linearly with the volume of the crystal, and start at photon energies that depend on the band structure of the material. However, they can also be used for our advantage in a photocatalytic context, as we will comment when discussing carrier injection. Then, metal NPs have two main modes of interaction with light. A collective response of their free carriers, which can support plasmonic resonances driven by an external field, and a single-electron response where carriers from low-lying, fully occupied bands are optically promoted to vacant states. This distinction is illustrated in Figure 1.3b, which shows two extinction spectra for a small gold NP, one obtained by using the experimental permittivity of bulk gold [37] and a second one with a permittivity obtained by modeling only its free carriers in the conduction band, using the Drude model. We describe this model in more detail in the next section, as we discuss the internal dynamics of the collective oscillation modes and how the electromagnetic energy of the driving field is moved into different degrees of freedom of the system.

1.2 Dynamics of Plasmon Excitation and Decay

1.2.1 Collective Charge Dynamics

In this section, we will describe the characteristics of carrier dynamics in a plasmonic oscillation, which will give us the opportunity to examine the different mechanisms by which the coherent oscillation can dephase. As discussed in the previous section, the materials that support a plasmonic oscillation are conductors. Therefore, they have a band that is only partially full, where the quasifree electrons can move in reaction to the external field. Within this context, interband transitions that overlap with the plasmonic resonance will be presented as another dephasing

mechanism. In modeling the behavior of the carriers in the conduction band, we start by considering an infinite, boundless gas of free electrons. Of course, this model can be connected with a realistic metal when we consider electron quasiparticles instead, which behave as free electrons with an effective mass $m \neq m_0$ that depends on the curvature of the band, with m_0 being the mass of a free electron in vacuum. These carriers, being fermions, occupy states of growing energy, E, following Fermi–Dirac statistics characterized by the distribution:

$$f_{\mathrm{F}} = \frac{1}{1 + e^{(E-E_{\mathrm{F}})/k_{\mathrm{B}}T}}. \tag{1.1}$$

Here T and k_{B} are the temperature of the system and the Boltzmann constant, respectively. In such a system, the Fermi energy, E_{F}, is a critical magnitude, indicating the energy of the highest occupied electronic state at $T = 0$ K. At nonzero temperatures, the electrons spread across the states with energies around this value, following Eq. (1.1). An equivalent picture can be presented in terms of their momentum, which will be useful in discussing the excitation of the gas by external fields. For free electrons, their energy is a direct function of their linear momentum p, expressed in terms of the electron wavenumber k as $E_k = \hbar^2 k^2/2m$, where $\hbar k = p$. We can thus derive a Fermi wavenumber from the Fermi energy, $k_{\mathrm{F}} = \sqrt{2mE_{\mathrm{F}}}/\hbar$. So, let us now consider a three-dimensional gas of free electrons in this representation, where the concept of Fermi surface corresponds to a spherical surface of constant wavenumber containing the occupied electronic states at equilibrium (assuming $T = 0$ K to simplify its description). A two-dimensional representation of this idea is presented in Figure 1.4a. In this figure, the black circle centered at $\mathbf{k} = 0$ is the Fermi surface at equilibrium. When an external electric field $\mathbf{E}$ interacts with the electrons, these will gain momentum in the axis containing the polarization of the field. This

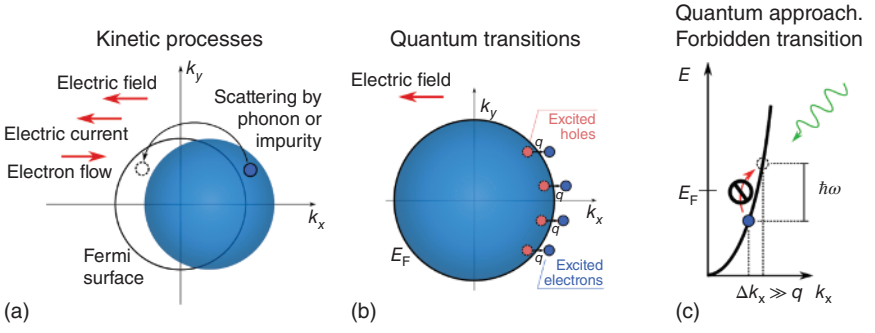

Figure 1.4 Free electron model in a system without boundaries. (a) Classical picture of the electron gas. Fermi sea in momentum space. The Fermi sea at equilibrium (empty black circle) is displaced by an external electric field, and the scattering of electrons with the crystal impose a friction-like force on their movement. (b) Quantum picture of the electron gas. Excitation of a Fermi sea by an external classical field. Each excited electron acquires a momentum $\hbar q$, with q being the wave vector of the external field, and a small amount of energy. (c) Diagram illustrating the impossibility of a mobile electron in the conduction band absorbing a photon in the quantum picture. The required change in its linear momentum is much larger than that carried by the photon. *Source*: Panels (a)–(c) were adapted with permission from Ref. [33] Copyright 2019 American Chemical Society.

is depicted in Figure 1.4a, where the large blue circle represents the Fermi sea and its displacement occurs in response to a field $\mathbf{E} \parallel -\hat{\mathbf{x}}$. The resulting displacement in the momentum space generates an electron flow and, consequently, a current. It is worth mentioning that this current will be finite, i.e. the acceleration of the charges by the field will be compensated by scattering events, like the one depicted in the diagram, until reaching a steady state.

In this picture, the particles in the electron gas are excited collectively. One can easily extend it to a situation where the external field oscillates harmonically, as $\mathbf{E}(t) = \mathbf{E}_0 e^{-i\omega t}$, such that the sphere of occupied electronic states will also oscillate in the same axis that the driving field does. This picture is a useful representation of the charge dynamics of a 3D degenerate gas of electrons under weak optical excitation. This is also a good framework to discuss the Drude model under a semiclassical perspective. Let us start by considering the average electronic velocity in the Fermi sea. By symmetry considerations, it is evident that this will be zero for the undisturbed electron gas, but it will increase as an external electric field displaces the sphere of occupied states in the reciprocal space. We express the change of the average velocity of the electron gas in terms of the balance between the driving force of the oscillating field and the opposing friction-like effect of electronic scattering, as

$$m\frac{d\overline{\mathbf{v}}}{dt} = e\mathbf{E} - m\ \gamma_D\ \overline{\mathbf{v}},$$

where $\gamma_D = 1/\tau_D$ is the effective scattering rate of electrons with the crystalline matrix and other electrons. From this framework we can recover the expression for the Drude permittivity of a metal [1, 34, 38]. For this we have to, again, consider that the average velocity of the electrons follow the same harmonic relationship as the field, to obtain its expression in the frequency domain

$$\overline{\mathbf{v}}_\omega = \frac{e\mathbf{E}_0}{m\left(\gamma_D - i\omega\right)}.$$

At this point, we can calculate the electrical conductivity predicted by the Drude model, σ_D, through Ohm's law and then use it in the expression for the complex-valued permittivity, $\varepsilon_D = \varepsilon_c + i\sigma_D/\omega\varepsilon_0$, to obtain Drude's expression for the permittivity

$$\varepsilon_D = \varepsilon_c - \frac{\omega_p^2}{\omega\left(\omega + i\gamma_D\right)}, \qquad \omega_p^2 = \frac{e^2 n_0}{\varepsilon_0 m}.$$

This expression includes the term ε_c to account for the optical response of lower-energy bands in the material, n_0 is the charge density in the conduction band, and ε_0 is the permittivity of free space.

In order to progress toward a more realistic description of the charge dynamics in a metal, especially if we are concerned with the description in microscopic systems, we should adopt explicitly quantum descriptions. In the first place, we can discretize the electronic transitions in the Fermi gas. Each electronic state is characterized by a wave vector $\mathbf{k}$, and an external electric field with wave vector $\mathbf{q}$ will be responsible for triggering the electronic transitions between states. Figure 1.4b depicts schematically the excited Fermi sea under this perspective, where the quantized electron gas

is excited by a classical external field. Using the random phase approximation (RPA) to simplify the many-body interaction in this framework, one arrives at Lindhard dielectric function [39, 40]

$$\varepsilon_{\mathrm{L}}(\omega, q) = \varepsilon_{\mathrm{c}} - \frac{e^2}{\varepsilon_0 q^2 V} \sum_k \frac{f_{\mathrm{F}}\left(E_{\mathbf{k}}\right) - f_{\mathrm{F}}\left(E_{\mathbf{k+q}}\right)}{\hbar\omega - E_{\mathbf{k+q}} + E_{\mathbf{k}} + i\hbar\gamma_{\mathrm{rel}}},$$

where V is the crystal's volume, $f_{\mathrm{F}}(\boldsymbol{E}_{\mathbf{k}})$ and $E_{\mathbf{k}}$ are the Fermi distribution function and the electron energy corresponding to the wave vector $\mathbf{k}$, respectively, and γ_{rel} is the phenomenological electronic relaxation rate. Here each electron changes its linear momentum by $\hbar q$ and gains a small amount of energy, i.e. the fastest electrons remain close to the Fermi surface (see Figure 1.4b). The currents generated by the collective excitation of the single carriers give rise to the plasmonic oscillation, similar to the previously described case.

Now, in a fully quantum-mechanical description of the system, we also have to consider the quantization of the external field. Under such perspective, the electrons are illuminated by discrete photons with energy $\hbar\omega$ and wave vector $\mathbf{q}$. Importantly, in this description of light interacting with the free electron gas (or equivalently, and more pertinently to our interests, the quasifree conductive electrons in a metal), we encounter that the absorption of a photon is impossible. Figure 1.4c illustrates this idea. Fundamentally, the small energy dispersion of the conduction band does not offer any available end state satisfying $E_{\mathbf{k}+\mathbf{q}} - E_{\mathbf{k}} = \hbar\omega$ [41], and for that transition to be possible the electron would either require to acquire additional momentum (through, e.g. inelastic scattering with a defect or a phonon), or occur in a confined system with boundaries. This latter situation is of particular relevance in the context of studying plasmonic resonances in nanostructures.

1.2.2 Confined Systems

After this progressive introduction to the dynamics of charge carriers in a metal through the exploration of a boundless electron gas, we can now discuss specific details of what happens when we consider finite systems, including the effects of confinement in small particles. The first immediate consequence of this transition is that the current created by the driving field will accumulate electric charge at the surface of the particle (inset in Figure 1.5a). In an ideal classical perspective, these charges would accumulate solely at the surface of the particle, but in realistic systems the charges at the interface extend into a non-zero volume inside the metal, screened and in interaction with other mobile charges. As we approach small particle sizes and electrons are not well approximated as point-like particles anymore, we can see Friedel oscillations caused by electron interference in the charge distribution close to the surface (see Figure 1.5b), which acts as a disturbing impurity [40, 44]. It is therefore not surprising that, as we decrease the size of the particle, the quantum effects at the surfaces become more relevant over the plasmon dynamics. In particular, they contribute to its dephasing, with the coherent collective oscillation of the carriers in the metal decaying into incoherent electronic excitations. This is observable through the broadening of the plasmonic peak in small NPs, with an increased

plasmon decay rate scaling as the inverse of their size [45, 46],

$$\gamma_{\text{surf}} = A \cdot \frac{v_{\text{F}}}{D},$$

where A is a numerical constant, D stands for the particle's diameter, and v_{F} is the Fermi velocity of the metal. Figure 1.5c illustrates such a trend for silver NPs in different substrates [43], but this is a general property that broadens the resonant peak in small particles of different materials [43, 46–50]. One can interpret this phenomenon either classically, arising from the collisions of ballistic electrons with the boundaries of the NC [51, 52], or in terms of quantum mechanics, as the boundary discretizes the electronic states inside the metal [45, 46, 52, 53]. Then, the surfaces allow the breaking of the momentum conservation described above (Figure 1.4c) by discretizing the electronic states in the particle, in what is known as surface-assisted plasmon decay or Landau damping. An important consequence of this is that particles' surfaces allow the excitation of high-energy HEs (Figure 1.5a,d), with energies up to the total photon quantum $\hbar\omega$ [53, 54], even in crystals with no defects and assuming an absence of electron–phonon interaction. Then, in the context of plasmonic photocatalysis, the surface effect in the plasmon dephasing is of particular importance because it is responsible for the internal generation of high-energy hot charge carriers in a manner that we can affect by controlling the shape and size of the metallic particle (Figure 1.5a,d). We should also bear in mind that another factor allowing the promotion of electrons to high-energy states is the existence of strong field gradients in the electromagnetic "hot spots" of the material [23, 55]. These are also related to the surface of the particles, more specifically to its shape and local curvature [54, 56], but hot spots can also arise by the near-field interaction of two or more plasmonic particles [55, 57–59], as we will see in more detail when discussing near-field enhancement.

1.2.3 Plasmonic Decay Channels

In this section, we have discussed the fundamental carrier dynamics in a plasmonic resonances, and we have described how these can decay through electron scattering and surface damping. In later sections of this chapter, we will discuss additional damping mechanisms for the plasmon, both internal and also depending on its environment. Before doing so, here we present a summary of the processes limiting the lifetime of the plasmon. Jointly, all of them contribute to broadening the plasmon resonance, and can be counted toward the total decay rate of the plasmon:

$$\gamma_{\text{plasmon}} = 1/\tau_{\text{plasmon}} = \gamma_{\text{NC}} + \gamma_{\text{rad}} + \gamma_{\text{env}}.$$

In this equation, we have separated the decay processes between those which are internal to the particle (γ_{NC}), those where the plasmon decays while exciting its immediate environment (γ_{env}), and the radiative losses (γ_{rad}). In Figure 1.6a, we provide a summary diagram of the rates involved in the plasmon and single-particle dynamics inside the particle. For the internal losses, we should distinguish between bulk mechanisms and those arising from the geometry of the nanostructure [23, 54].

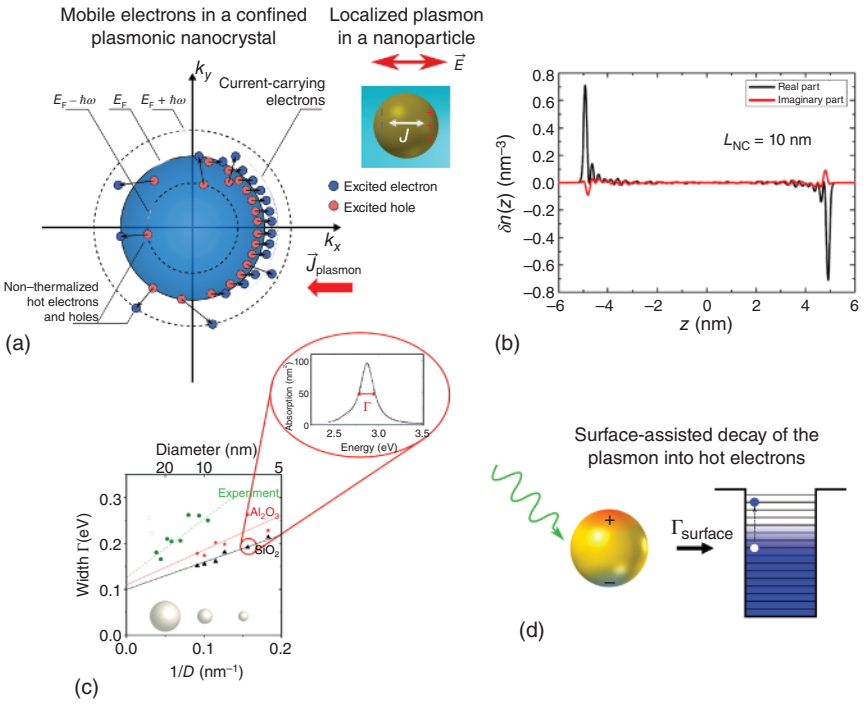

Figure 1.5 Effects of boundaries in the plasmon dynamics. (a) Excitation of the Fermi sea in a metal NP. Carriers can now be excited to energies up to the total energy of the photon thanks to their interaction with the particle's surface. (b) Real and imaginary part of the nonequilibrium complex electron density in an optically excited gold slab. We can see Friedel oscillations next to its surfaces. (c) The surface broadening of the optical features of an NC increase with decreasing particle size. (d) Diagram of the surface-assisted promotion of high-energy electrons. The presence of the surface allows the absorption of a photon by a single electron, breaking the limitation depicted in Figure 1.4c. *Source*: Adapted with permission from Refs. (a) [33] Copyright 2019 American Chemical Society, (b) [42] Copyright 2015 American Chemical Society, (c) [43] Copyright 2011 American Chemical Society, (d) [23] Copyright 2019 Elsevier.

The latter allow the internal generation of HEs, either because of the change of linear momentum allowed by the surfaces, γ_{surf} (Figure 1.6b), or because of the strong internal field gradients in hot spots, $\gamma_{\text{hot spot}}$:

$$\gamma_{\text{NC}} = \gamma_{\text{bulk}} + \gamma_{\text{surf}} + \gamma_{\text{hot spot}},$$

and where the decay channels relating to the bulk material are further subdivided into two terms:

$$\gamma_{\text{bulk}} = \gamma_{\text{Drude}} + \gamma_{\text{interband}},$$

one for the rate of electron–electron and electron–phonon scattering, γ_{Drude}, which enters the description of the system under the Drude model to give a friction-like force relaxing the electronic momentum (Figure 1.6b); and another quantifying the rate of optical interband transitions, $\gamma_{\text{interband}}$(Figure 1.6b) [1]. Lastly, we also include

the effects of the environment into the decay of the plasmon,

$$\gamma_{\text{env}} = \gamma_{\text{charge transfer}} + \gamma_{\text{near field}},$$

where the $\gamma_{\text{charge transfer}}$ term refers to processes where an electron is promoted from the particle into a excited state in the environment, or vice versa, be it in an adsorbed molecule or an interfacing semiconductor. Lastly, the $\gamma_{\text{near field}}$ term would quantify the decay rates arising from the near-field coupling of the plasmonic NC with another system.

The collective electronic oscillation that is sustained in a metallic particle when exciting a plasmonic resonance stores energy in a relatively ordered many-body state. As this phenomenon, involving the coherent motion of carriers, interacts with the material supporting it or its environment, this energy will degrade until it diffuses as heat (Figure 1.6c). However, most of these decay mechanisms provide ways for the plasmonic NP to share its energy or charge with other material elements in the system. By using plasmonic NPs in a photocatalytic context, we aim to create a reactor in which other elements can efficiently utilize this energy in subsequent chemical transformations, so that we can direct its flow as it proceeds downstream in terms of its coherence. In the rest of the chapter we will explore different mechanisms that can make this possible.

1.3 Hot Electrons: Energy Distribution and Mechanisms of Generation

As the coherent plasmonic oscillation evolves in time and loses energy to single-electron states, several types of excited electrons coexist inside the particle, characterized by their energies and their origin. The first kind, and most common, are the electrons that carry the current of the plasmonic oscillation and have small energies above the Fermi energy (see Figure 1.5a). These are found in the large peaks with energies just above E_{F} in Figure 1.7a, and we refer to them as Drude electrons, with the equivalent populations with energies below E_{F} being Drude holes. This figure shows a diagram with the general features appearing in the change in electronic occupation, with respect to the equilibrium population at room temperature, in the steady state of a small Au NP excited at its plasmonic resonance in the linear regime, i.e. with relatively low light fluxes [33, 54]. The other main feature in this plot is the quasiflat population that extends to carrier energies up to the total energy of the incoming photons. These are HEs and HHs that can be excited due to the interaction of the plasmon with the surfaces of the NP, and to which we refer as nonthermal hot carriers, because their populations cannot be well described by an effective temperature. These arise in systems with boundaries that break the translational symmetry of the material, allowing for the electron scattering that permits the full absorption of the photon. Another important category of excited carriers are the thermalized HEs, which also contribute to the main low-energy peaks in Figure 1.7a. As the nonthermal HEs lose energy via rapid electron–electron scattering, they become thermalized HEs, contributing with the

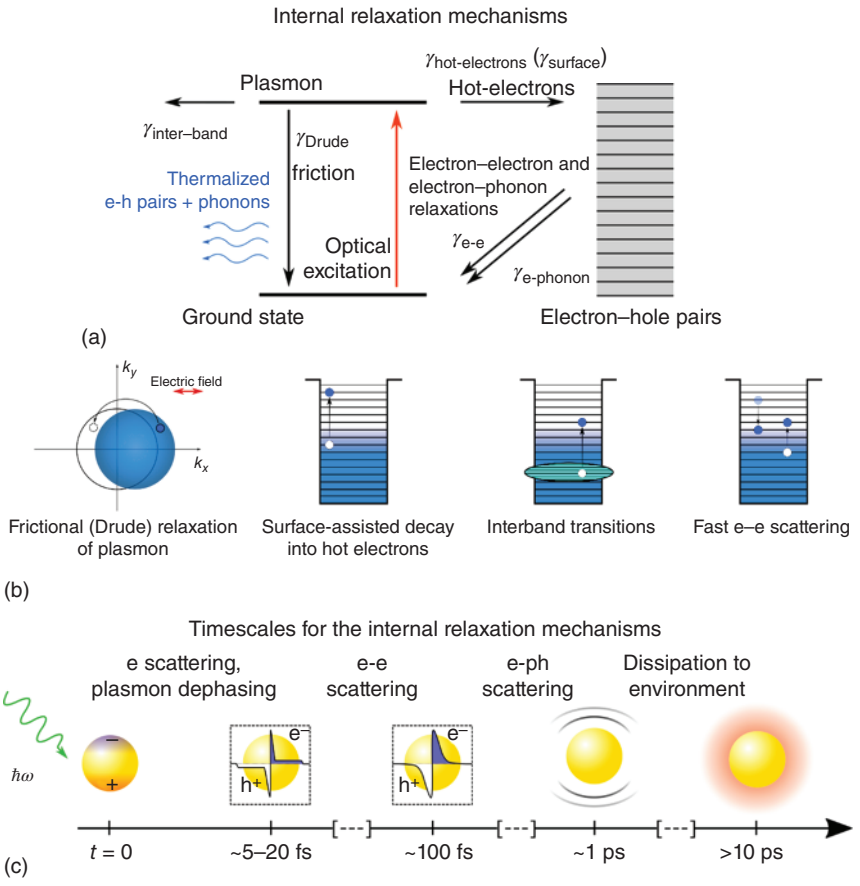

Figure 1.6 (a) Internal channels for the decay of the plasmon in an NC, as well as single-particle relaxation mechanisms. (b) Schematic diagram of the main mechanisms depicted in panel a. The first three are channels for plasmon decay, which transfer energy to single-particle states, while the fourth is the main relaxation mechanism for high-energy HEs and HHs. (c) Diagram with the sequence of dominant mechanisms involved in plasmon decay and electronic relaxation, indicating at which approximate timescales after excitation they become relevant. Of course, this picture presumes a pulse excitation, and under continuous illumination all of these processes happen concurrently, achieving a nonequilibrium steady state that balances Eq. (1.2). *Source*: Adapted with permission from Refs. (a) [54] Copyright 2017 American Chemical Society, (b) [33] Copyright 2019 American Chemical Society, (c) [23] Copyright 2019 Elsevier.

Drude electrons to an excited population that can be described by an effective electronic temperature T_e, higher than that of the atomic lattice [23].

Developing the notion of these electronic subsystems within the plasmonic NP, several multitemperature models have been proposed to characterize its internal time dynamics. In Figure 1.7b, we illustrate the main elements of our proposed quantum two-temperature (Q2T) model [23], which expands on existing extended 2 T models [60–64]. This panel illustrates the distinct subsystems, the couplings between them, and the energy inputs to the system. The Q2T model codifies this information

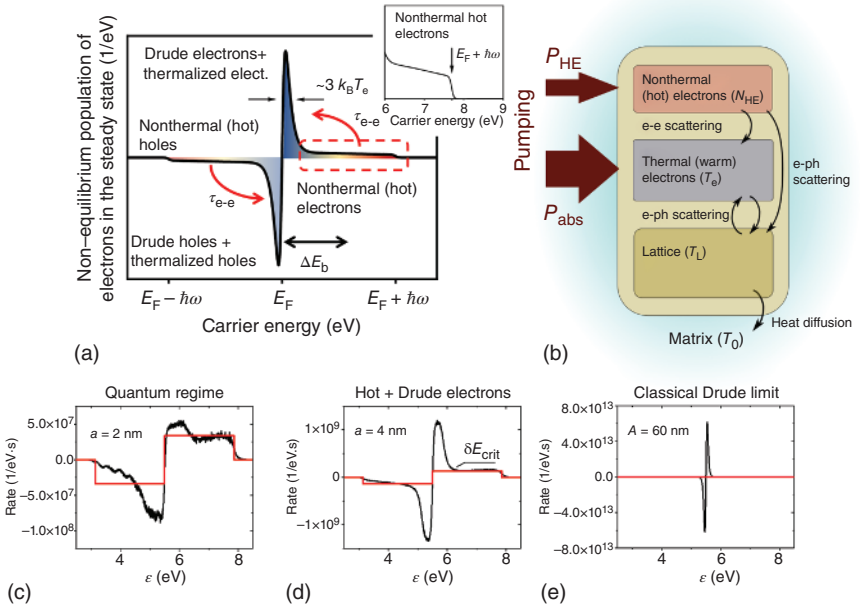

Figure 1.7 (a) Typical distribution of excited electrons in an optically driven plasmonic NC under continuous illumination. There are two types of carriers: low-energy electrons and holes (Drude-like and thermalized) and nonthermal high-energy HEs and HHs. The latter can have up to the total energy of the photon (see inset). Here, T_e is the effective temperature of the optically driven Fermi gas, and τ_{e-e} is the average time between electron–electron scattering events that distribute and homogenizes their energies. (b) Diagram with the different subsystems exchanging energy in a plasmonic nanostructure, as well as the relevant energy inputs and output. This diagram corresponds to the quantum 2 T model [23], a revision to previous extended 2 T models [60–64]. (c–e) Profiles for the rates of excitation of electrons in gold NPs of different diameters. Each particle is excited at its plasmonic resonance by light with a flux of $I_0 = 3.6 \times 10^3$ W/cm^2. The surface-assisted excitation of HEs and HHs is prominent for small NPs, but its relative relevance decreases with the reduction of the particle's surface-to-volume ratio. For larger sizes we recover the behavior of a classical plasmon, with negligible rate of HE and HH excitation. *Source*: Adapted with permission from Refs. (a) [33] Copyright 2019 American Chemical Society, (b) [23] Copyright 2019 Elsevier, (c) [54] Copyright 2017 American Chemical Society.

in the following set of coupled equations, accompanied by full description of the notation used:

$$\begin{aligned}
\frac{dE_{HE}}{dt} &= -a_{e-e}E_{HE} + P_{HE} \\
\eta_e T_e \frac{dT_e}{dt} &= -G\left(T_e - T_L\right) \\
&\quad + a_{e-e}E_{HE} + P_{abs} \\
C_L \frac{dT_L}{dt} &= G\left(T_e - T_L\right) \\
&\quad - C_L \frac{T_L - T_0}{\tau_{heat\ \ transfer}}
\end{aligned}
\qquad
\begin{cases}
E_{HE} \equiv \text{total energy of nonthermalized HEs in NC} \\
T_e \equiv \text{electronic temperature} \\
T_L \equiv \text{lattice temperature} \\
T_0 \equiv \text{ambient temperature} \\
a_{e-e} \equiv \text{e} - \text{e relaxation rate of HEs} \\
P_{abs} \equiv \text{classical optical absorption rate of NC} \\
P_{HE} \equiv \text{power exciting HEs} \\
G \equiv \text{e-ph coupling constant} \\
C_e = \eta_e T_e \equiv \text{electronic heat capacity of NC} \\
C_L \equiv \text{lattice heat capacity of NC;} \quad C_L >> C_e \\
\tau_{heat\ \ transfer} \equiv \text{time of heat transfer NC} \rightarrow \text{matrix}
\end{cases}
\tag{1.2}$$

We should note that the above equation is written only for the intraband excitations and, therefore, it is applicable for Au NCs with plasmonic resonances in the red region such as nanorods, nanocubes, and nanostars. It can also be applied to Ag NCs and other plasmonic systems whose plasmonic resonance does not overlap with the interband transitions of the material. For spherical Au NCs, one needs to modify the above equations to account for the interband transitions. The physical significance of most of the variables involved should be clear by contrasting the equations with Figure 1.7b, but it is worth making explicit the expressions for the two terms that model the energy input to the system. The classical absorption rate contributes directly to the effective electronic temperature, and it is calculated as the time-averaged losses arising from the electron scattering described by the Drude model:

$$P_{\text{abs}} = \left\langle \int_{\text{NC}} \mathrm{d}V \ \mathbf{j}\cdot\mathbf{E} \right\rangle_{\text{time}} = \text{Im}\left(\varepsilon_{\text{Drude}}\right) \frac{\omega}{8\pi} \int_{\text{NC}} \mathrm{d}V \ \mathbf{E}_{\omega}\cdot\mathbf{E}_{\omega}^{*},$$

while the generation of nonthermal HEs should be calculated following a quantum formalism as [54, 65]

$$P_{\text{HE}} \approx \frac{1}{4}\frac{2}{\pi^2} \times \frac{e^2 {E_{\text{F}}}^2}{\hbar} \frac{1}{(\hbar\omega)^2} \int_{S_{\text{NC}}} \left| E_{\omega,\text{normal}}\left(\mathbf{r}\right)\right|^2 \mathrm{d}s, \tag{1.3}$$

where $E_{\omega,\,\text{normal}}$ is the electric field inside the particle and normal to its surface, and the physical field is defined here as $\mathbf{E} = \text{Re}\,\mathbf{E}_{\omega}\mathrm{e}^{-i\omega t}$. Again, the generation of nonthermal HEs, with energies up to the total energy of the photon, is allowed by the surface effect discussed above. Without it this transition would be forbidden, as it is the case for a free electron (Figure 1.4c). As a consequence of this, small particles with large surface-to-volume ratios will use a larger proportion of the total absorbed power, $P_{\text{abs}} + P_{\text{HE}}$, to excite nonthermal HEs, in comparison to Drude electrons. The three last panels in Figure 1.7 show precisely this, by contrasting side to side the theoretical rates of intraband carrier excitation for three different sizes of spherical gold NPs as a function of carrier energy. While for the large particle the volume effect dominates and almost all carriers are excited with low energies around E_{F}, the balance changes as we decrease the particle size, until we reach a system where the nonthermal HEs are excited at rates comparable with the Drude-like carriers. From Eq. (1.3) we also learn that the amplitude of the electric field at the surfaces of the particle is key to increase the rate of generation of HEs, so plasmonic hot spots will increase the number of hot carriers in the particle. We will discuss electromagnetic hot spots in more detail in the section dedicated to coherent energy transfer.

It is important to note, in the context of the transfer of energy between subsystems in the plasmonic particle (Figure 1.7b), the relevant timescales for the different transitions. Figure 1.6c illustrates the evolution of a plasmonic NP excited by a pulse excitation [23]. In particular, after the rapid dephasing of the plasmon into a population of single-electron states, their relaxation through electron–electron scattering

will proceed at rates that depend on their energy

$$a_{\mathrm{e-e}} \approx \frac{1}{\tau_{\varepsilon,\mathrm{e-e}}(\varepsilon)}, \qquad \tau_{\varepsilon,\mathrm{e-e}}(\varepsilon) = \tau_{0,\mathrm{e-e}} \frac{E_{\mathrm{F}}^2}{\left(\varepsilon - E_{\mathrm{F}}\right)^2}, \tag{1.4}$$

where $\tau_{0,\,\mathrm{e-e}}$ is a constant depending on the metal. The expression for $\tau_{\varepsilon,\,\mathrm{e-e}}$ in Eq. (1.4) holds for Fermi liquid theory [66], and entails that high-energy electrons will lose energy very rapidly, after a few collisions [67]. At this point, the relaxation of the thermalized excited carriers, sharing their energy with the crystalline matrix, will be controlled by electron–phonon scattering events, which occur at a significantly slower rate than electron–electron collisions, $\tau_{\varepsilon,\,\mathrm{phonons}} \gg \tau_{\varepsilon,\,\mathrm{e-e}}$. Of course, the picture described in Figure 1.6c corresponds to a pulse excitation. This is useful to understand the carrier dynamics inside the particle, but in general we will be interested in the steady state under continuous illumination when studying photocatalysis. In the steady state, the nonthermal hot carriers will coexist with thermalized hot carriers, as more are continuously excited and the system continues to dissipate energy into the crystalline matrix and its environment. It is important, however, to keep in mind the short lifetimes of the nonthermal hot carriers, as this will limit the probability of them leaving the plasmonic particle before thermalizing.

1.4 Charge Transfer Mechanisms Associated with Plasmons

We have seen how, as the plasmon dephases inside a plasmonic NP, its energy is distributed among single-electron degrees of freedom. Some of these charge carriers can be transferred to the environment, either reaching molecular adsorbates directly [17] or using semiconductor catalysts in an intermediate charge separation step [15]. The consequent ionization of the molecules can contribute to drive redox processes [68, 69], or excite vibrational states through an intermediate charged excited state in what is often referred as desorption induced by electronic transition (DIET) [70–72]. In contrast with the thermal activation of the reaction, on which we will comment in more detail later in the chapter, charge transfer mechanisms can offer access to new reaction products, as well as product selectivity [73–76]. Although the transfer processes are concurrent with the heating by the plasmonic particle, and they can act synergistically [73, 77–79], it is in principle possible to estimate their relative contributions to the reaction rates [78, 80]. For instance, two properties have been used to recognize charge transfer processes in experimental photocatalytic systems with metal NPs: the transition from linear to superlinear dependence of the reaction rates with light's intensity as multitransfer events become more probable [17, 81], and the higher rates induced in reactions with lighter isotopes [17, 22]. Beyond these, additional procedures have been proposed for teasing apart the relative importance of hot carrier injection and photoheating in driving chemical reactions. [82]

Although charge transfer mechanisms play an important role in the effective design of plasmonic photocatalytic systems, the efficiencies achieved to date with systems exploiting them remain low [83]. There are different paths that can lead to

larger efficiencies, such as tailoring the plasmonic system to increase its generation rates of high-energy electrons. This can be done by considering shapes and sizes that maximize the surface-mediated promotion of these carriers [23], or creating electromagnetic hot spots through particle–particle interaction [55, 57] or the particle's curvature [65]. But in addition to studying the efficiency of these systems in generating such excited carriers capable of migrating out of the plasmonic particle, we should pay close attention to the injection process itself. Now, in order to discuss the mechanisms of charge transfer between plasmonic particle and environment, it is useful to consider the distinction between indirect and direct carrier transfer. In the former the electronic transition is internal to the metal and a secondary injection step is required, while in the latter the dephasing of the plasmon triggers an electronic transition between the metal particle and the environment.

1.4.1 Indirect Hot Carrier Injection

We can start by briefly discussing the indirect injection of excited carriers, as it follows straightforwardly from the discussion in the previous section. In it, we discussed how the decay of the plasmon populates a collection of excited electronic states, including both low- and high-energy carriers. Now, for any of these to contribute to the photocatalytic process, they need to leave the particle. A fraction of them will be injected into the environment, a process labeled as "indirect" because it represents an independent step from the excitation of the carrier. The energy of the internally excited carrier is very relevant in processes of indirect injection, because in general there will be a potential barrier that the carriers need to surpass to be ejected from the particle (Figure 1.8a) [84–86]. For metal–semiconductor interfaces, the relevant concept is that of a Schottky barrier [87]. This barrier resulting from the bending of the semiconductor bands when it contacts the metal has two effects: first, it prevents low-energy excited carriers to leave the metal; second, it limits the back-transfer of charge carriers injected from the metal, making semiconductors useful for limiting the rapid relaxation of high-energy electrons in the metal. One should note, however, that different combinations of materials can result in ohmic contacts or small Schottky barriers at their interfaces, opening new possibilities in designing efficient photocatalytic reactors [88]. Furthermore, by creating electrically gated devices, it is possible to actively control the barrier's height and thus filter carrier injection. [89] The simplest approach to quantifying the amount of excited carriers that will traverse the interface is to just consider whether they have enough kinetic energy to surpass the barrier. This approach sets a threshold value on the carrier's energy for its injection, but ignores consideration of the electron's momentum at the interface and can therefore only give us a ceiling on the real injection rates. The diagram in Figure 1.8a shows the energy barrier height ΔE_b, setting this threshold. Under this perspective, any estimation of the injection rate should include some function of the overbarrier energy, $\hbar\omega - \Delta E_b$ [65, 67, 84, 86].

More detailed models for electronic injection through a Schottky barrier take into account other factors limiting electron transmission at the interface. For instance, energy profile and width of the potential barrier should be considered in order

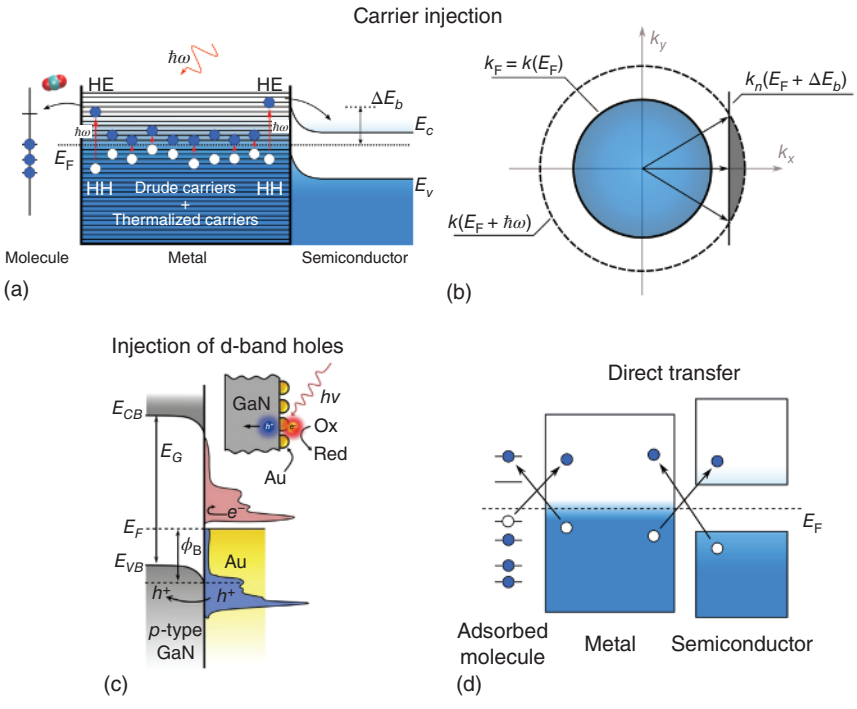

Figure 1.8 (a) Diagram showing the different types of excited carriers inside a NP under optical excitation. The carriers with enough energy to traverse the potential barriers at the boundaries of the NP are susceptible of being injected into its environment. (b) Diagram of electron injection in momentum space. The inner circle represents the ground state of the Fermi sea, and the dashed circle marks the maximum momenta of optically driven electrons. The grayed-out section contains the excited electrons satisfying, within the Fowler theory, the condition for injection at a boundary extending along the *yz* plane. The function used in the panel computes the wave number as $k(E) = \sqrt{2mE/\hbar^2}$, and $k_n(E)$ denotes the component of the wave vector normal to the surface. (c) Diagram illustrating the injection of holes into a *p*-type semiconductor. Although HEs and HHs are also generated here through plasmonic excitation, by illuminating at a wavelength that permits interband transitions of electrons from the *d*-band, one can obtain large numbers of high-energy HHs [19]. (d) A direct transfer to the environment is also possible, contrasting with the indirect, two-step injection shown in panels (a)–(c). If the plasmonic NP is in contact with a material providing an external density of states, be it an adsorbed molecule or an adjacent semiconductor, the plasmon can decay by exciting a single carrier across the two systems. An electron excited in such a way can go from the metal to the neighbor, or from the external system into the metal, resulting in the latter case a hole injection to the adsorbate or semiconductor. *Source*: Adapted with permission from Refs. (a) [23] Copyright 2019 Elsevier, (c) [19] Copyright 2018 American Chemical Society.

to account for the possibility of tunneling by electrons with lower energies than ΔE_b, although this is only be relevant for very thin interfacial regions [87]. More commonly, the study of photoinjection at Schottky barriers takes a ballistic model of the electron and examines the limitations that the barrier imposes on an injection event so that it respects both energy and momentum conservation. This is the

framework under which the Fowler theory models the photoinjection in thick films [90]. Figure 1.8b shows a geometrical interpretation of the momentum conservation constraining the injection, which defines a region of allowed momenta by imposing the condition $(\hbar k_n)^2/2m > E_F + \Delta E_b$ for injection, where k_n is the component of the carrier's wave vector normal to the barrier [91]. The probability of carrier injection according to Fowler theory is of the form

$$\eta_{\text{Fowler}} \propto \frac{\left(\hbar\omega - \Delta E_b\right)^2}{\hbar\omega E_F}.$$

Extensions of this model use semiclassical methods to include additional considerations, like multiple electron reflection at surfaces, to explain the enhanced injection observed in Schottky photodetectors with thin metal films [92, 93]. It should be noted that these models of injection typically assume the generation of high-energy electrons across the volume of the metal, not only at its surfaces [94]. A complete account of the photoinduced injection at a Schottky barrier should also consider these carriers and their drift inside the particle. However, in the previous section of the chapter we have focused on the generation of HEs through a surface-assisted mechanism. This is so because this is the fundamental quantum mechanism that can provide high-energy carriers in a plasmonic resonance, and is dominant for small NPs [94]. Nonetheless, we direct the interested reader to a recent detailed discussion of these and other factors in Ref. [67].

A similar discussion can be presented for the case of molecules adsorbing to the plasmonic material. In this context, the threshold to the injection of excited carriers results from the alignment between the electronic states of metal and the hybridized electronic states of the adsorbed molecule. If the lowest unoccupied molecular orbital (LUMO) has a higher energy than the metal Fermi level, the electrons in the metal will require additional energy to reach it. Therefore, one can also consider an energy-threshold approach to find upper bounds for the rates of injection to adsorbates. Of course, in real systems there are also more factors playing a role in regulating the electronic injection from plasmonic NCs to molecules, such as the affinity of the molecule to the different crystal facets of the particle [95], and the details of the hybridization of states between metal and molecule [74].

At this point, it is useful to refer again to the interband transitions occurring in metals (Figure 1.3c). As mentioned in the introduction, the part of the absorption spectrum due to interband transitions cannot be tuned through changes in the geometry of the NP. Nonetheless, given the large density of states in the *d*-bands of noble metals, the absorption from interband transitions can also be large, and they can be useful in a photocatalytic context. Given that the *d*-bands in plasmonic materials are deep below the Fermi energy, optically excited electrons originating in them will have low kinetic energies, while the corresponding holes will be very energetic. Therefore, one can devise photocatalytic schemes that take advantage of this situation. As an example, Figure 1.8c illustrates a photoelectrochemical system using a *p*-type semiconductor that can extract the energetic holes, while the excited electrons drive CO_2 reduction [19]. High-energy HHs, either in the conduction band or in the *d* band, can also target the direct molecular oxidation of adsorbates while exciting the plasmonic NP at low wavelengths [20, 96].

1.4.2 Direct HE Injection

In addition to the internal decay of the plasmon into single-electron states, we should take into account that the dephasing of the plasmon is also influenced by the environment of the plasmonic structure. In particular, when the NP is in contact with the electronic density of states of an adjacent semiconductor or adsorbed molecule, the energy of the plasmon can trigger electronic transitions that cross the interface of these materials, in what is often referred to as direct charge transfer events [97–99]. From the perspective of an optical analysis of the plasmonic NCs, these mechanisms can become apparent as the additional broadening of the plasmon resonances in the spectrum of the sample, and was therefore included in our general discussion on the plasmon decay rate, γ_{plasmon}, as $\gamma_{\text{charge transfer}}$. This is a general term that aims to group what in the literature is typically referred to as chemical interface damping (CID) [100, 101] and plasmon-induced interface charge transfer [97], depending on whether the transfer occurs with adsorbed molecules or adjacent semiconductors, respectively. Its magnitude will depend on the materials composing the plasmonic particle and its neighbor, as well as on their surface and interfacial electronic states.

In contrast with the previously discussed indirect charge transfer, this is a process that excites a charge carrier into the particle's environment in a single step, instead of a two-step excitation–injection process. Therefore, this charge transfer connects a donor (acceptor) state in the plasmonic particle with an acceptor (donor) state in its environment, be it in an adsorbed molecule [99, 101, 102] or in an adjacent semiconductor [97–99] (Figure 1.8d). An important implication of this distinction is that the excited electron or hole does not stay for any length of time inside of the metal, where it can lose its energy before being able to leave the particle, due to the rapid scattering events with other electrons (see Figure 1.6c). In other words, this type of hot carrier excitation has an intrinsic 100% injection efficiency, and designing plasmonic catalysts with interfaces that promote this effect would be very desirable. This can prove to be a challenging goal, given the difficulty to experimentally distinguish between mechanisms of carrier injection, although it has been suggested that polarization-dependent injection efficiency in metal–QD junctions could be evidence of direct HE injection [97]. Therefore, most current efforts for understanding this mechanisms are theoretical, including the use of atomistic ab initio methods to probe the charge dynamics of coupled metal–semiconductor [98] or metal–molecule [99] systems. Interestingly, recent theoretical results suggest that upward of 40% of total plasmonic decay in small Ag NPs coupled to CdSe NPs, under pulsed excitation, is due to direct transfer [98]. This is a very promising result, inviting more research toward the possibility of exploiting this mechanism in practical setups to enhance the overall efficiency of plasmonic photocatalysis.

1.5 Plasmonic Near-Field Enhancement

As discussed in the introduction, the resonant coherent charge oscillation of a plasmon results in the generation of a strongly enhanced electric field inside

and near the particle [1]. This stronger field can boost optical and photocatalytic processes in molecules or QDs nearby the plasmonic particle (Figure 1.9). A commonly mentioned example of this phenomenon is surface-enhanced Raman spectroscopy (SERS), an early application of plasmonics in modern scientific practice. It exploits the field enhancement of a surface plasmon supported by a metallic surface to increase the Raman signal of its molecular adsorbates, leading to large enhancements due to the nonlinear dependency of Raman scattering on the intensity ($\propto|\mathbf{E}|^4$) [106, 107]. Therefore, SERS benefits from the design of plasmonic systems with strong near fields (see Figure 1.9a) [103]. Other processes that can be enhanced by a strong plasmonic near field are fluorophore and semiconductor emission [108–111], photon upconversion [112–114], molecular chiral signal [115, 116] or, importantly, photocatalysis [18, 104, 105, 114], where the energy receptor can be molecules (Figure 1.9b) or semiconducting crystals (Figure 1.9c).

The local enhancement factor is a useful magnitude for quantifying the local strengthening of the field with respect to the background illumination, and is defined as

$$P_{\text{local}}(\mathbf{r}) = \frac{\left|\mathbf{E}_{\omega}(\mathbf{r})\right|^2}{E_0^2},$$

where $\mathbf{E}_{\omega}(\mathbf{r})$ is the total complex-valued electric field and E_0 is the amplitude of the impinging radiation. Using this magnitude, it is easy to characterize the near-field enhancement of different plasmonic NPs, which is relevant to understand the impact of the particle's geometry to the spatial distribution and strength of its near field. The image in Figure 1.10a maps the values of $\sqrt{P_{\text{local}}(\mathbf{r})}$ for a cross-section of a spherical Au NP of 10 nm in diameter, thus showing the enhancement on the electric field's amplitude. It is strongest along the direction of polarization of light, as it excites the particle as a dipole antenna, and decays rapidly as we get away from the surface of the particle [1, 117]. It is also worth noting that the enhancement factor is greater than one inside the particle, which is a signature of the resonant excitation that drives the internal energy dissipation and excitation of hot carriers. The geometry of a plasmonic NC influences its near field in terms of form and intensity. Most notably, it can give rise to electromagnetic hot spots, regions with a particularly large electric field amplitude. Hot spots appear at sharp features in a particle, because the small local radius of curvature does increase the local surface charge density. Figure 1.10b presents such an example, where we can see the hot spots that result at the sharp edges of an Au nanocube. Although real nanocubes cannot have perfectly sharp edges, they nonetheless show strong hot spots at edges and corners [118–120]. Metallic nanostars are another good example of this type of hot spots [121], and one that has also been shown to be useful in a photocatalytic context by increasing the internal generation rates of HEs [122]. Hot spots also appear where the near field of two or more plasmonic NPs interact. Figure 1.10c exemplifies this with a dimer of 10 nm Au spheres. These are the same NPs as the one shown in Figure 1.10a, but the increased field strength at the dimer gap is apparent, with an approximate five-fold increase between the strongest points in each map. Of course, one can create plasmonic systems combining these two types of hot spots, such as in the so-called

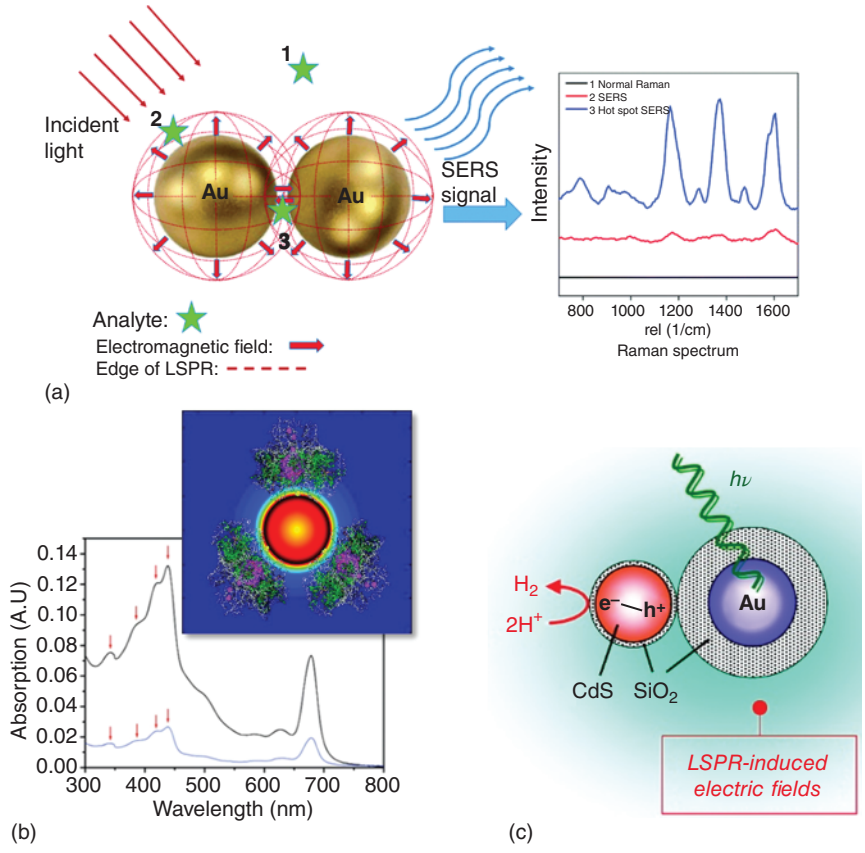

Figure 1.9 (a) Plasmonic systems increase the molecular signal in Raman spectroscopy through near-field enhancement, so that plasmonic hot spots are especially effective. Plasmonic field enhancement can also drive photocatalytic processes, by exciting neighboring molecules and semiconducting QDs. (b) Comparison between the absorption of suspensions of photosynthetic protein Photosystem I (PS I), unbounded (blue curve) and bounded to Ag NPs (black curve). The top inset depicts PS I molecules attached to a plasmonic NP. The background color gradient represents the enhancement factor of the NP, which is strongest close to the NP. (c) Schematic diagram of a system designed for enhancing the photocatalytic properties of CdS QDs with the near field of Au NPs. Both particles are separated by a SiO_2 layer preventing charge transfer between them. *Source*: Adapted with permission from Refs. (a) [103] published by the Royal Society of Chemistry, (b) [104] Copyright 2010 American Chemical Society, (c) [105] Copyright 2011 American Chemical Society.

bowtie antennas, a commonly used system designed to study the effect of plasmonic hot spots [57, 59, 123].

Given the strong decay of the enhanced near field with the distance from the particle's surface ($\propto 1/r^3$ for the dipolar plasmonic modes), it is clear that we will be interested in positioning the acceptor system as closely as possible to the plasmonic particle. But doing this also come at a disadvantage. Balancing enhancement and quenching is crucial to efficiently promote photoemission in fluorophores with plasmonic NCs, as their nonradiative losses increase when they come too close

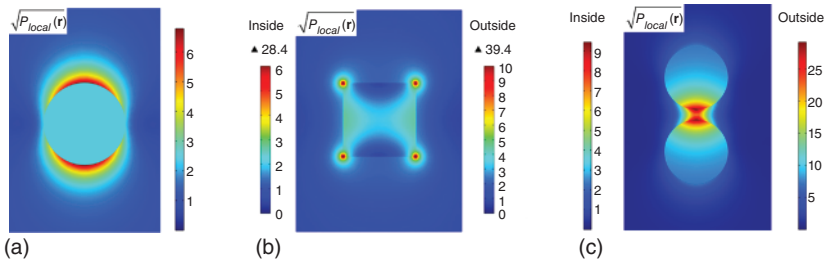

Figure 1.10 Enhancement factor maps of Au NCs with different geometries, immersed in water and excited at their resonant frequencies. (a) Au sphere with a diameter of 10 nm. (b) Au cube with an edge length of 7 nm, with strong hot spots at its vertices. This cube has sharp edges, in order to demonstrate the limits of near-field enhancement through increased surface curvature. (c) Dimer composed by 2 Au NPs of 10 nm in diameter, separated by a gap of 1.7 nm. Although the constant curvature of the spheres does not create hot spots, as in panel (a), the interaction between both generates a very strong hot spot at the gap. *Source*: Panel (b) was adapted with permission from Ref. [54] Copyright 2017 American Chemical Society.

to the NC and dominate over the radiative decay rates [124–126]. Consequently, it is common practice to use dielectric spacers to reduce nonradiative losses in systems of plasmonically enhanced photoemission [127, 128]. Similarly, while the enhanced near field can boost the absorption of a nearby molecule, if it comes in contact with the metal the latter can also act as an electron drain and decrease the final reaction yield. Then, photocatalytic strategies that rely on the coherent near-field excitation by the plasmonic particle can also use spacers to prevent the possibility of charge exchange with the plasmonic material [18, 105]. As we have seen in previous sections, charge transfer is an important mechanism in plasmonic catalysis, but whether is advantageous or disadvantageous will depend on different factors, including the relative energy alignment between the electronic states of the catalyst and the reactants.

Lastly, processes that are enhanced by the increased amplitude of the plasmonic near field will have to be not only spatially but also spectrally close to the resonance. The situation is slightly different, however, in the case of the near-field enhancement of the processes in other conductive particles [129, 130] or in multimetallic particles [131]. The strong, oscillating near field of the plasmonic NP will create currents in the other conductive material, or effectively resonate together in a hybrid coupled mode, and this excitation will drive catalytic activity at the surface of these nonplasmonic metal particles. In this case, the plasmonic resonance does not need to be close to, for instance, the absorption lines of the molecule, because the conducting co-catalyst mediates in the transfer. Taken as a single catalytic unit, the hybrid multimetallic system would work in a way more closely resembling monometallic plasmonic hot carrier injection, while providing additional control over reaction selectivity [132, 133].

1.6 Plasmonic Scattering

Let us now consider a mechanism of plasmonic decay connecting the particle with the far field, instead of with its immediate environment. In the same way that the

plasmon can be excited by an incoming plane wave, it can re-radiate electromagnetic energy in the reciprocal process. This process, to which we typically refer to as radiative decay or plasmonic scattering, is perhaps the one for which the analogy of a plasmonic NP as an antenna is most clarifying. In the same way that macroscopic antennas show reciprocity between reception and transmission, the dipolar modes excited in a plasmonic system can radiate back into space. For plasmonic NPs, an important property to note is that their scattering cross-sections depend strongly on their geometry and size, so that small particles can radiate back a negligible amount of energy, even though they show a significant coupling with incoming light because of their plasmonic resonance. Looking at the expression of classical absorption and scattering cross-sections for small particles will help us discuss this more precisely.

Absorption and scattering cross-sections quantify the proportion of the incident light flux that is dissipated inside the particle and reradiated, respectively. Therefore, $\sigma_{\text{abs}} = P_{\text{abs}}/I_0$ and $\sigma_{\text{scat}} = P_{\text{rad}}/I_0$, where P_i stands for power, absorbed and radiated, and I_0 is the incident light's intensity. If we assume that the particle is much smaller that the wavelength of light, we can approximate its response as that of a point dipole, in what is known as the quasistatic limit or approximation. In such a case, it is useful to characterize a NC simply through its polarizability, $\alpha = \mu/E$, which tells us how strong an electric dipole μ is induced by the external field. We can then express both absorption and scattering cross-sections of an arbitrary small particle as a function of its polarizability [134, 135]

$$\sigma_{\text{abs}} = \frac{4\pi k}{\varepsilon_{\text{env}}} \text{Im}\left[\alpha\right], \qquad \sigma_{\text{scat}} = \frac{8\pi\, k^4}{3} |\alpha|^2,$$

where ε_{env} is the permittivity of the environment where the particle is embedded. The polarizability of a particle will depend on its shape, but for spherical systems it simple scales linearly with its volume. Therefore, for spherical particle of small sizes (e.g. low tens of nanometers for Au), the linear term on the volume, absorption, will dominate over the quadratic, scattering. At larger sizes, this trend will reverse. Of course, satisfying the quasistatic approximation means that we are also within the Rayleigh scattering limit, with its familiar $1/\lambda^4$ dependency, so that scattering will be more relevant at high frequencies. So, materials with large plasma frequencies, such as Al, will scatter more strongly that materials such as Au, which resonate in the visible to IR region. We should also remember that even small particles can show significant scattering cross-sections if they have large aspect ratios, as is the case of NRs, and therefore a larger polarizability than spheres of equivalent volume. Although far from being complete, this short discussion should give some intuition for the relevant factors impacting scattering on small plasmonic NPs, and the interested reader can learn more about the radiative properties of plasmonic systems in other resources on the topic [1, 135, 136].

Now, to consider how plasmonic scattering can play a role in photocatalytic strategies, we have to consider that, although the reemission will be biased toward the direction of the incoming light, the scattered photons will in general travel along a different path than the incoming radiation [136, 137]. Therefore, the presence of scatterers in a medium will increase the effective optical thickness of a system, as sketched in Figure 1.11a. As such, plasmonic NPs can be of use in photocatalytic [16] and photovoltaic [138, 139] systems, with the goal of achieving significant light

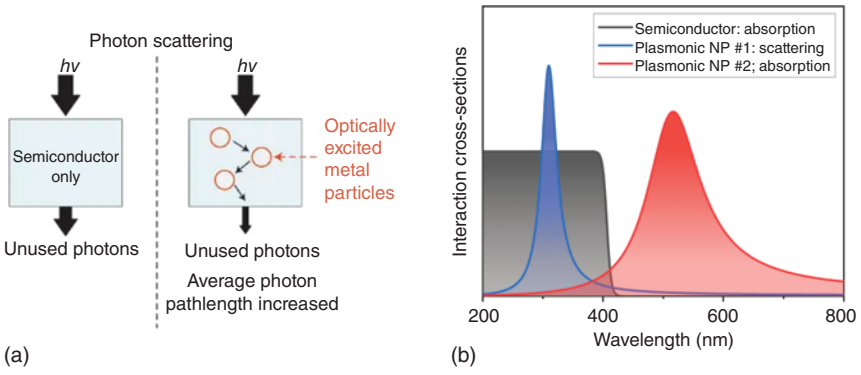

Figure 1.11 (a) Scattering plasmonic nanoparticles can be used to extend the effective optical thickness of an optically active material or device. However, for this mechanism to be useful, these particles need to scatter light at frequencies that the surrounding medium can absorb. In panel (b) we contrast this situation, in the context of a semiconducting absorbing material (modeled with the bandgap of TiO_2), with that of using other mechanisms like charge transfer or photoheating, where the plasmonic resonance does not need to overlap with the semiconductor's absorption. Consequently, using plasmonic nanoparticles purely as scatterers can increase the optical thickness of a system, but not its operative spectrum. *Source*: Panel (a) was adapted with permission from Ref. [16] Copyright 2011 Springer Nature.

absorption with thinner layers of material. It is important to keep in mind, however, that scattering is an elastic process, so the reemitted photons will have the same energy than those exciting the plasmonic resonance. Therefore, using plasmonic NPs effectively as scatterers depends on the presence of other mechanisms converting light's energy into a form that is useful for the chemical process. This can be either accomplished at the plasmonic NP itself – absorption and scattering can coexist in a particle resonating at a given wavelength, i.e. a fraction of the interacting photons will be absorbed – or by optical absorption events at the molecules or co-catalysts. An enhancing strategy that uses plasmonic NPs only as scatterers will then typically require that they operate at high frequencies, where other elements in the system can absorb the scattered photons. Figure 1.11b illustrates this situation in the context of a semiconductor medium, and contrasts it with an approach where the plasmonic NP uses other mechanisms to transfer energy – such as HEs or photoheating – in a manner that takes advantage of regions of the spectrum unavailable for direct absorption in the semiconductor.

1.7 Photoheating

Heating always occurs when we illuminate plasmonic NPs, as the energy of the plasmonic resonance dissipates internally due to electrons scattering with the atomic lattice of the metal. The previously discussed mechanisms can extract part of this energy and transfer it to other elements in the environment before this happens, contributing to the reaction [17, 69, 78]. But, of course, photoheating is also a useful process and can contribute to drive the chemical process through an increase in

local temperature, and the nonthermal mechanisms discussed above can also be understood as acting in reducing the activation energy of the reactions, so that they can proceed at lower temperatures [77–79, 140]. Moreover, even plasmonic NPs used exclusively as nanoheaters can provide significant efficiencies in setups designed around this strategy, e.g. exploiting photogenerated temperature gradients where the resulting thermophoretic forces separate the reaction products from the active reaction sites [141].

When considering plasmonic heating as a photocatalytic mechanism, we have two main ways of describing the local effects of the plasmonic NC, depending on whether we focus on the phononic or electronic transfer of energy. In the first case, we can simply consider the plasmonic NP as a dissipative system, behaving like a localized photoheater [142]. As the metal particle is illuminated, it will heat up and raise its temperature and that of other materials with large thermal conductivity in contact with it. The environment is subsequently heated up due to the photoinduced temperature gradient. Figure 1.12a shows the steady state temperature obtained by illuminating an isolated gold NP immersed in water. The increase in temperature outside a small isolated particle follows the expression [142]

$$\Delta T(r) = \frac{V_{\mathrm{NP}} Q}{4\pi k_0 r},$$

where V_{NP} is the volume of the particle, Q is the total heat it dissipates, k_0 is the thermal conductivity of the environment, and r is the distance to the center of the particle. With each particle serving as a photoheater, the macroscopic local temperature will increase at a rate controlled by the optical and thermal properties of the ensemble and matrix, as well as the light's intensity [7, 142, 144–146]. In Figure 1.12b, we can see theoretical values comparing the temperature increase of one particle and a small ordered ensemble of 16 NPs. Of course, one can also exploit interaction effects between plasmonic NPs, effectively creating a more efficient photothermal metamaterial [7]. Figure 1.12c exemplifies this with a model system created to study the effect of interparticle interaction in ensemble photoheating [143], but one can also create photoheaters by considering ordered planar structures functioning as perfect absorbers [5, 147].

On the second perspective, we can evaluate the thermal effects of plasmonic NPs insofar they impact charge exchanges with their environment, under a perspective that connects directly with the one used to describe the mechanisms of HE injection [33]. For this, we can consider the energy distribution of the carriers inside the plasmonic NP, and how the temperature of the lattice affects their injection possibilities in two different contexts. In the first, the electrons in the particle are separated from their environment by a relatively high potential barrier of $\Delta E = 0.8$ eV, a value compatible with typical values of Au and Ag Schottky barriers [84]. In such a situation, the total energy of a plasmon excited in the visible or near-IR spectral range would be sufficient to drive charge injection into its environment, be it through direct promotion or through the two-step process illustrated in Figure 1.13a. On the contrary, if in the context of a large barrier we consider electronic occupation of states through Fermi–Dirac statistics at the temperature of the lattice, the probability of injection will be very small [68]. Again, for a barrier $\Delta E = 0.8$ eV, the probability of injection would be in the order of 10^{-14} at low light fluencies, a situation in which the

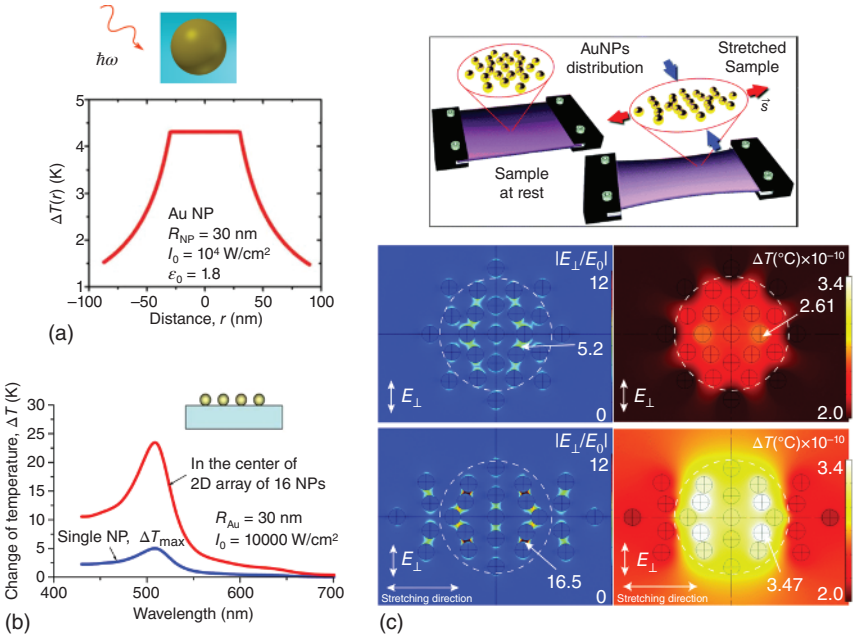

Figure 1.12 Plasmonic nanoparticles as photoheaters. (a) Single particle. Diagram of an optically excited gold nanoparticle immersed in water, and theoretical data of the temperature increase inside and around it as a function of the distance to its center. (b) Collective heating. Increasing the number of photoheaters will increase the heat deposited in the region, leading to higher phototemperatures. Comparison between the temperature increase of a single NP and a 4×4 NP planar array. (c) Electromagnetic coupling. Two or more plasmonic nanoparticles in close interaction will create hot spots that enhance the total absorption in the spheres, with the consequent increase in dissipated heat. The top schematic diagram shows an experimental setup used to quantify the effect of electromagnetic coupling between AuNPs on photoheating. The four lower panels show theoretical data for such a system, with field enhancement maps on the left and temperature maps on the right. The data in the top row shows the results under no tension, while the bottom row correspond to a stretched system. The dashed line outlines the laser beam spot. *Source*: Adapted with permission from Refs. (a) [142] Copyright 2007 Elsevier, (b) [7] Copyright 2006 Springer, (c) [143] Copyright 2018 Royal Society of Chemistry.

particles remain relatively close to room temperature. And although the probability of injection will of course increase when considering a hotter system, for realistic temperatures in colloidal systems, the energy of these thermalized electrons will remain significantly lower than the energy barrier, $T_e \ll \Delta E_b/k_B$. For this barrier height, one could estimate that the thermionic electrons would compare with the number of over-barrier plasmonic HEs only at $T_e \sim 500$ K, by using the expressions in Figure 1.13a,b [33]. On the other hand, other material combinations offer small potential barriers between metal and environment, such as the TiN/TiO_2 ohmic junction reported in Naldoni et al. [88]. In such a case, illustrated in Figure 1.13c, the picture is notably different, and realistic increases in the effective electronic temperature for nonconcentrated solar radiation can still notably increase the number of carriers that can leave the plasmonic NC.

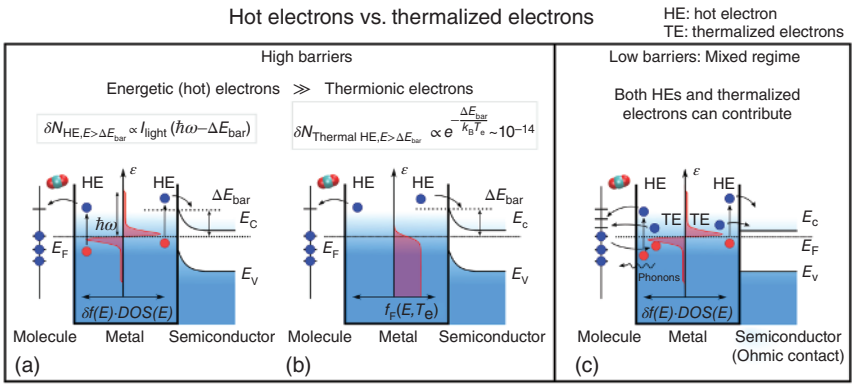

Figure 1.13 Comparison of thermal effects and indirect HE injection. These illustrations sketch the fundamental differences between the impact of thermalized and nonthermalized carriers toward charge injection, in two distinct situations at the metal–environment interfaces: having a high (panels a and b) or low (panel c) potential energy barrier. (a) Diagram focusing on the internal generation of hot carriers. The injection barrier is significantly larger than the effective electron temperature T_e, i.e. $\Delta E_{bar} > > k_B T_e$. The function inside the metal shows the distribution of nonequilibrium electrons in a metal under optical excitation. The number of HEs with energies $E > \Delta E_{bar}$ is linearly proportional to the intensity of light. (b) Still assuming a high barrier, we show the distribution of carriers inside a photoheated metal, under low-intensity illumination. We assume that its temperature is higher than room temperature by 20 K. The probability of injection over a barrier scales exponentially, and it is very low for realistic values of Schottky barrier (we take $\Delta\varepsilon_{bar} = 0.8$ eV, as in an Au–TiO_2 interface). (c) In the case of low interfacial barrier, such as that of TiN–TiO_2 junctions [88], both high-energy HEs and thermalized electrons are susceptible of being injected to the environment and contribute to the reaction. Regardless of barrier height, the crystal heats the environment through the exchange of phonons. We illustrate this in panel c only, to simplify the overall presentation. *Source*: Adapted with permission from Ref. [33], Copyright 2019 American Chemical Society.

1.8 Example Applications

The mechanisms discussed here provide different opportunities for using plasmonic NCs to our advantage in photocatalytic and photoelectrocatalytic systems, enabling different strategies for the pursuit of greater efficiencies in the light-assisted catalysis of chemical reactions of technological relevance. In this section, we will briefly describe different applications, including some on which other chapters will expand upon, that highlight the relevance of specific ideas discussed in this chapter. Perhaps most notably, plasmonic NPs have been proposed as useful tools driving solar water splitting for the clean production of hydrogen fuel [21, 152], CO_2 reduction [153, 154], and nitrogen fixation [141, 155], but the list of potential applications is much broader [22, 156, 157]. Across these, plasmonic NPs can be exploited in different ways. A well-known strategy is the combination of different materials to create hybrid reactors, with a prime example being the loading of Au NPs in TiO_2 to enhance the charge separation capabilities of the semiconductor and target specific reactions [15]. Other material combinations have also shown great promise, including the use of plasmonic NPs with good catalytic metals, such as Pt and Pd [129, 131, 158–161], with semiconductor nanostructures [16, 157, 162–164], or with

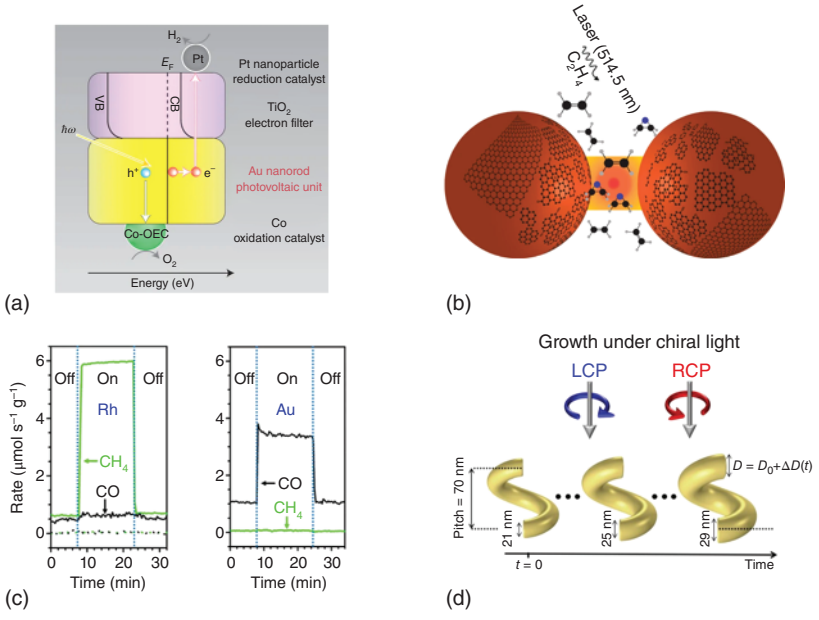

Figure 1.14 (a) Autonomous water-splitting photocatalytic unit, where charge carriers are generated in a Au NR and different materials separate and direct them to distinct reaction sites [148]. (b) Schematic diagram of the photocatalytic formation of graphene on Ag nanoparticles, as an intermediate process promoting ethylene epoxidation [149]. (c) Results from photocatalytic systems for CO_2 hydrogenation using Rh or Au NPs, showing a strong product selectivity. (Left) Rates of production of CO and CH_4 in the dark and under UV light, using Rh. (Right) Rates of production of CO and CH_4 in the dark and under white light, using Au [150]. (d) Diagram depicting hot-electron induced growth of metallic crystals, which can be controlled through the circular polarization of light when using chiral plasmonic nanostructures [151]. *Source*: Adapted with permission from Refs. (a) [148] Copyright 2013 Springer Nature, (b) [149] Creative Commons Attribution 4.0 International License, (c) [150] Creative Commons Attribution 4.0 International License, (d) [151] Copyright 2020 American Chemical Society.

materials offering rapid carrier extraction and transport, such as CNTs [165, 166]. An interesting example of this kind of strategies is the work presented by Mubeen et al. [148], where a complex of four materials is used to complete both oxidation and reduction steps in water splitting (Figure 1.14a). A gold NR is used to collect radiant energy within a broad range of wavelengths, up to the near-IR, and the excited electron and holes are routed to two distinct reaction sites functionalized with two different catalytic materials, each targeting specific semireactions of water splitting.

This serves as a reminder of the crucial importance of the detailed surface characteristics at the active reaction elements, which are critical for targeting a given chemical reaction. Among the many ways of exemplifying the nontrivial dependency on the catalyst's surface, let us briefly look at studies of metal catalysts in ethylene epoxidation, another chemical reaction of societal significance [167]. Silver is a common catalyst used in temperature-driven ethylene epoxidation [167, 168], and the shape of nanostructures of this metal – determining the crystal facets contributing to the reaction – was shown to be relevant for controlling the

selectivity of this catalytic process [95]. Silver was subsequently shown to also be effective as a photocatalyst in enhancing this reaction [156]. Interestingly, Zhang et al. have recently presented results showing that, in the photocatalytic epoxidation of ethylene using Ag NPs, the reaction proceeds through an intermediate step synthesizing graphene at the NPs' surfaces (Figure 1.14b), which mediates the injection of HEs photoexcited at the NP and whose defects become the reaction sites for the epoxidation [149]. Such results invite the question of whether we could design different complexes with advanced surface functionalization that improves the efficiency of different plasmonic photoreactors.

Plasmonic particles also facilitate the design of photocatalytic systems with product reaction selectivity. This is a property that we have not explored in depth in this chapter, but it is nonetheless of great importance in practical applications. The spectral tunability of plasmonic structures, in combination with material-dependent properties such as its work function and crystalline surface facets, make them a versatile tool for targeting specific reaction paths [17, 22, 169]. As an example, we can highlight the work by Zhang et al., where they contrast the evolution of systems with either Rh or Au NPs loaded on Al_2O_3 supports for the hydrogenation of CO_2 [150]. Besides the overall increased efficiency of the photoexcited systems for both materials with respect to the thermal catalysis in dark conditions, the comparison between both photocatalysts showed that using Rh NPs offered a greater degree of control over the reaction products. As shown in Figure 1.14c, the CH_4 reaction path was substantially promoted over the CO path when the Rh-loaded system was illuminated. This kind of product selectivity is presumably allowed by the excitation of plasmonic hot carriers to promote the otherwise kinetically dispreferred reaction path [69, 75, 150, 170], and underscores the relevance of plasmonics in catalytic applications.

We can also gain additional degrees of control over a photocatalytic system by designing asymmetric plasmonic nanostructures. For instance, plasmonic structures with chiral geometries interact differentially to opposite polarizations of circularly polarized light (CPL) [171, 172]. The optical asymmetries that can be achieved with chiral plasmonic structures, measured through circular dichroism or through the dissymmetry or anisotropy factor g, greatly exceed those of chiral molecules. This is true for planar metamaterials [173–175], structured particle complexes [174, 176–179], and colloidal chiral particles [151, 172]. Therefore, using nanostructured metals we can also tailor the optical response of a photocatalytic system and engineer its response to circularly polarized light. It bears clarifying that these processes are fundamentally different from traditional chiral photocatalysis, which pertains to the differential synthesis of molecular enantiomers. On the contrary, these mechanisms are not intended to offer control over the chiral asymmetry of the molecular reaction, but to grant us another variable to control photocatalytic processes through the properties of incoming light. Recently, we have proposed this as a mechanism in surface photochemistry induced by CPL, to either control the evolution of chemical reactions downstream of the plasmonic excitation [175, 178] or trigger differential crystalline growth of chiral particles through their surface chemistry [151, 180]. Figure 1.14d schematically represents this idea, and stands as another example of a distinctive research direction associated with plasmonic catalysis.

1.9 Outlook

Plasmonic NPs offer a variety of ways to enhance photocatalytic processes. Their great spectral tunability and strong coupling with light make them excellent tools to either absorb light across the whole solar spectrum or to create custom spectral profiles to offer reaction selectivity. The stages in the life of a plasmon, from its initial excitation to the dissipation of its energy in the form of heat, offer different and distinct mechanisms for the transfer of its energy to the environment of the particle. This chapter has described the fundamental properties of plasmon dynamics in a metal NP and the associated energy-transfer mechanisms. Designing successful strategies for exploiting plasmonic materials in a photocatalytic context will depend on the careful design of hybrid systems that manage the flow of energy and charge from the resonant plasmonic modes to the molecular species. Having a detailed description of plasmonic dynamics and transfer mechanisms is crucial for such a design process, and we expect to see new exciting approaches and opportunities as we improve our theoretical understanding of these processes and this active field continues to develop.

Acknowledgements

We gratefully acknowledge the support provided by the following funding institutions. L.V.B, was supported by the Institute of Fundamental and Frontier Sciences, University of Electronic Science and Technology of China and the National Natural Science Foundation of China (12050410252). Z.M.W. was funded by the National Key Research and Development Program (No. 2019YFB2203400), the "111 Project" (B20030), and the UESTC Shared Research Facilities of Electromagnetic Wave and Matter Interaction (Y0301901290100201). A.O.G. was supported by the U.S.–Israel Binational Science Foundation (BSF).

References

1 Maier, S.A. (2007). *Plasmonics: Fundamentals and Applications*. New York: Springer.
2 Cai, W., Chettiar, U.K., Kildishev, A.V., and Shalaev, V.M. (2007). *Nat. Photonics* 1: 224–227.
3 Yu, N., Genevet, P., Kats, M.A. et al. (2011). *Science* 334: 333–337.
4 Khurgin, J.B. (2015). *Nat. Nanotechnol.* 10: 2–6.
5 Landy, N.I., Sajuyigbe, S., Mock, J.J. et al. (2008). *Phys. Rev. Lett.* 100: 207402.
6 Li, W. and Valentine, J.G. (2016). *Nanophotonics* 6: 177.
7 Govorov, A.O., Zhang, W., Skeini, T. et al. (2006). *Nanoscale Res. Lett.* 1: 84–90.
8 Hao, J., Zhou, L., and Qiu, M. (2011). *Phys. Rev. B* 83: 165107.
9 Wang, X., Li, G., Ding, Y., and Sun, S. (2014). *RSC Adv.* 4: 30375–30383.

10 Hogan, N.J., Urban, A.S., Ayala-Orozco, C. et al. (2014). *Nano Lett.* 14: 4640–4645.
11 Akbari, A., Tait, R.N., and Berini, P. (2010). *Opt. Express* 18: 8505.
12 Li, W. and Valentine, J. (2014). *Nano Lett.* 14: 3510–3514.
13 Kong, X.-T., Khosravi Khorashad, L., Wang, Z., and Govorov, A.O. (2018). *Nano Lett.* 18: 2001–2008.
14 Hung, W.H., Aykol, M., Valley, D. et al. (2010). *Nano Lett.* 10: 1314–1318.
15 Primo, A., Corma, A., and García, H. (2011). *Phys. Chem. Chem. Phys.* 13: 886–910.
16 Linic, S., Christopher, P., and Ingram, D.B. (2011). *Nat. Mater.* 10: 911–921.
17 Linic, S., Aslam, U., Boerigter, C., and Morabito, M. (2015). *Nat. Mater.* 14: 567–576.
18 Shaik, F., Peer, I., Jain, P.K., and Amirav, L. (2018). *Nano Lett.* 18: 4370–4376.
19 DuChene, J.S., Tagliabue, G., Welch, A.J. et al. (2018). *Nano Lett.* 18: 2545–2550.
20 Schlather, A.E., Manjavacas, A., Lauchner, A. et al. (2017). *J. Phys. Chem. Lett.* 8: 2060–2067.
21 Mascaretti, L., Dutta, A., Kment, Š. et al. (2019). *Adv. Mater.* 31: 1805513.
22 Gellé, A., Jin, T., de la Garza, L. et al. (2020). *Chem. Rev.* 120: 986–1041.
23 Besteiro, L.V., Yu, P., Wang, Z. et al. (2019). *Nano Today* 27: 120–145.
24 Fox, M.A. and Dulay, M.T. (1993). *Chem. Rev.* 93: 341–357.
25 Jiang, C., Moniz, S.J.A., Wang, A. et al. (2017). *Chem. Soc. Rev.* 46: 4645–4660.
26 Li, J. and Wu, N. (2015). *Cat. Sci. Technol.* 5: 1360–1384.
27 Kisch, H. (2017). *Acc. Chem. Res.* 50: 1002–1010.
28 Belver, C., Bedia, J., Gómez-Avilés, A. et al. (2019). *Nanoscale Materials in Water Purification*, 581–651. Elsevier.
29 Grätzel, M. (2001). *Nature* 414: 338–344.
30 Naik, G.V. and Boltasseva, A. (2010). *Phys. Status Solidi RRL - Rapid Res. Lett.* 4: 295–297.
31 Faucheaux, J.A., Stanton, A.L.D., and Jain, P.K. (2014). *J. Phys. Chem. Lett.* 5: 976–985.
32 Taliercio, T. and Biagioni, P. (2019). *Nanophotonics* 8: 949–990.
33 Chang, L., Besteiro, L.V., Sun, J. et al. (2019). *ACS Energy Lett.* 4: 2552–2568.
34 Tanner, D.B. (2019). *Optical Effects in Solids*. Cambridge: Cambridge University Press.
35 Govorov, A.O., Zhang, H., Demir, H.V., and Gun'ko, Y.K. (2014). *Nano Today* 9: 85–101.
36 Landau, L.D. and Lifshitz, E.M. (1976). *Mechanics*, 3e. Elsevier, Butterworth Heinemann: Burlington, MA.
37 Johnson, P.B. and Christy, R.W. (1972). *Phys. Rev. B* 6: 4370.
38 Wooten, F. (1972). *Optical Properties of Solids*. New York: Academic press.
39 Lindhard, J. (1954). *Dan. Mat.-Fys. Meddeleiser* 28: 1–57.
40 Mahan, G.D. (2000). *Many-Particle Physics*, 3e. Boston, MA: Springer US.
41 Ashcroft, N.W. and Mermin, N.D. (1976). *Solid State Physics*. New York: Holt, Rinehart and Winston.
42 Govorov, A.O. and Zhang, H. (2015). *J. Phys. Chem. C* 119: 6181–6194.

43 Lermé, J. (2011). *J. Phys. Chem. C* 115: 14098–14110.
44 Friedel, J. (1952). *Lond. Edinb. Dublin Philos. Mag. J. Sci.* 43: 153–189.
45 Kawabata, A. and Kubo, R. (1966). *J. Physical Soc. Japan* 21: 1765–1772.
46 Genzel, L., Martin, T.P., and Kreibig, U. (1975). *Z. Für Phys. B Condens. Matter Quanta* 21: 339–346.
47 Kreibig, U. and Genzel, L. (1985). *Surf. Sci.* 156: 678–700.
48 Link, S. and El-Sayed, M.A. (1999). *J. Phys. Chem. B* 103: 4212–4217.
49 Derkachova, A., Kolwas, K., and Demchenko, I. (2016). *Plasmonics* 11: 941–951.
50 Baida, H., Billaud, P., Marhaba, S. et al. (2009). *Nano Lett.* 9: 3463–3469.
51 Doremus, R.H. (1965). *J. Chem. Phys.* 42: 414–417.
52 Shahbazyan, T.V. (2016). *Phys. Rev. B* 94: 235431.
53 Manjavacas, A., Liu, J.G., Kulkarni, V., and Nordlander, P. (2014). *ACS Nano* 8: 7630–7638.
54 Besteiro, L.V., Kong, X.-T., Wang, Z. et al. (2017). *ACS Photonics* 4: 2759–2781.
55 Besteiro, L.V. and Govorov, A.O. (2016). *J. Phys. Chem. C* 120: 19329–19339.
56 Schuller, J.A., Barnard, E.S., Cai, W. et al. (2010). *Nat. Mater.* 9: 193–204.
57 Cortés, E., Xie, W., Cambiasso, J. et al. (2017). *Nat. Commun.* 8: 14880.
58 Negrín-Montecelo, Y., Comesaña-Hermo, M., Kong, X.-T. et al. (2018). *ChemCatChem* 10: 1561–1565.
59 Ding, W., Bachelot, R., Kostcheev, S. et al. (2010). *J. Appl. Phys.* 108: 124314.
60 Sun, C.-K., Vallée, F., Acioli, L.H. et al. (1994). *Phys. Rev. B* 50: 15337–15348.
61 Carpene, E. (2006). *Phys. Rev. B* 74: 024301.
62 Avanesian, T. and Christopher, P. (2014). *J. Phys. Chem. C* 118: 28017–28031.
63 Della Valle, G., Conforti, M., Longhi, S. et al. (2012). *Phys. Rev. B* 86: 155139.
64 Zavelani-Rossi, M., Polli, D., Kochtcheev, S. et al. (2015). *ACS Photonics* 2: 521–529.
65 Kong, X.-T., Wang, Z., and Govorov, A.O. (2017). *Adv. Opt. Mater.* 5: 1600594.
66 Pines, D. and Nozières, P. (1989). *Theory of Quantum Liquids*. Reading, MA: Addison-Wesley Pub. Co., Advanced Book Program.
67 Khurgin, J.B. (2020). *Nanophotonics* 9: 453–471.
68 Yu, S. and Jain, P.K. (2020). *Angew. Chem.* 132: 2101–2104.
69 Yu, S., Mohan, V., and Jain, P.K. (2020). *MRS Bull.* 45: 43–48.
70 Avouris, P. and Walkup, R.E. (1989). *Annu. Rev. Phys. Chem.* 40: 173–206.
71 Gadzuk, J.W. (1983). *J. Chem. Phys.* 79: 6341–6348.
72 Gadzuk, J.W. (2000). *Chem. Phys.* 251: 87–97.
73 Bonn, M. (1999). *Science* 285: 1042–1045.
74 Kale, M.J., Avanesian, T., Xin, H. et al. (2014). *Nano Lett.* 14: 5405–5412.
75 Landry, M.J., Gellé, A., Meng, B.Y. et al. (2017). *ACS Catal.* 7: 6128–6133.
76 Kumar, P.V. and Norris, D.J. (2017). *ACS Catal.* 7: 8343–8350.
77 Kim, Y., Dumett Torres, D., and Jain, P.K. (2016). *Nano Lett.* 16: 3399–3407.
78 Zhou, L., Swearer, D.F., Zhang, C. et al. (2018). *Science* 362: 69–72.
79 Gargiulo, J., Berté, R., Li, Y. et al. (2019). *Acc. Chem. Res.* 52: 2525–2535.
80 Kamarudheen, R., Castellanos, G.W., Kamp, L.P.J. et al. (2018). *ACS Nano* 12: 8447–8455.
81 Olsen, T. and Schiøtz, J. (2009). *Phys. Rev. Lett.* 103: 238301.

82 Baffou, G., Bordacchini, I., Baldi, A., and Quidant, R. (2020). *Light Sci. Appl.* 9: 108.

83 Ratchford, D.C. (2019). *ACS Nano* 13: 13610–13614.

84 Sze, S.M. and Ng, K.K. (2007). *Physics of Semiconductor Devices*, 3e. Hoboken, NJ: Wiley-Interscience.

85 Govorov, A.O., Zhang, H., and Gun'ko, Y.K. (2013). *J. Phys. Chem. C* 117: 16616–16631.

86 Knight, M.W., Sobhani, H., Nordlander, P., and Halas, N.J. (2011). *Science* 332: 702–704.

87 Tung, R.T. (2014). *Appl. Phys. Rev.* 1: 011304.

88 Naldoni, A., Guler, U., Wang, Z. et al. (2017). *Adv. Opt. Mater.* 5: 1601031.

89 Sistani, M., Bartmann, M.G., Güsken, N.A. et al. (2020). *ACS Photonics* 7: 1642–1648.

90 Fowler, R.H. (1931). *Phys. Ther. Rev.* 38: 45–56.

91 Mooney, J.M. and Silverman, J. (1985). *IEEE Trans. Electron Devices* 32: 33–39.

92 Vickers, V.E. (1971). *Appl. Optics* 10: 2190.

93 Dalal, V.L. (1971). *J. Appl. Phys.* 42: 2274–2279.

94 Brown, A.M., Sundararaman, R., Narang, P. et al. (2016). *ACS Nano* 10: 957–966.

95 Christopher, P. and Linic, S. (2010). *ChemCatChem* 2: 78–83.

96 Peng, T., Miao, J., Gao, Z. et al. (2018). *Small* 14: 1703510.

97 Wu, K., Chen, J., McBride, J.R., and Lian, T. (2015). *Science* 349: 632–635.

98 Kumar, P.V., Rossi, T.P., Marti-Dafcik, D. et al. (2019). *ACS Nano* 13: 3188–3195.

99 Kumar, P.V., Rossi, T.P., Kuisma, M. et al. (2019). *Faraday Discuss.* 214: 189–197.

100 Hövel, H., Fritz, S., Hilger, A. et al. (1993). *Phys. Rev. B* 48: 18178.

101 Foerster, B., Joplin, A., Kaefer, K. et al. (2017). *ACS Nano* 11: 2886–2893.

102 Therrien, A.J., Kale, M.J., Yuan, L. et al. (2019). *Faraday Discuss.* 214: 59–72.

103 Wei, H., Hossein Abtahi, S.M., and Vikesland, P.J. (2015). *Environ. Sci. Nano* 2: 120–135.

104 Carmeli, I., Lieberman, I., Kraversky, L. et al. (2010). *Nano Lett.* 10: 2069–2074.

105 Torimoto, T., Horibe, H., Kameyama, T. et al. (2011). *J. Phys. Chem. Lett.* 2: 2057–2062.

106 Gersten, J. and Nitzan, A. (1980). *J. Chem. Phys.* 73: 3023–3037.

107 Schatz, G.C. (1984). *Acc. Chem. Res.* 17: 370–376.

108 Munechika, K., Chen, Y., Tillack, A.F. et al. (2010). *Nano Lett.* 10: 2598–2603.

109 Okamoto, K., Niki, I., Shvartser, A. et al. (2004). *Nat. Mater.* 3: 601–605.

110 Akselrod, G.M., Argyropoulos, C., Hoang, T.B. et al. (2014). *Nat. Photonics* 8: 835–840.

111 Srinivasan, V. and Ramamurthy, S.S. (2016). *J. Phys. Chem. C* 120: 2908–2913.

112 Wu, D.M., García-Etxarri, A., Salleo, A., and Dionne, J.A. (2014). *J. Phys. Chem. Lett.* 5: 4020–4031.

113 Park, W., Lu, D., and Ahn, S. (2015). *Chem. Soc. Rev.* 44: 2940–2962.

114 Xu, Z., Quintanilla, M., Vetrone, F. et al. (2015). *Adv. Funct. Mater.* 25: 2950–2960.

115 Lieberman, I., Shemer, G., Fried, T. et al. (2008). *Angew. Chem. Int. Ed.* 47: 4855–4857.

116 Govorov, A.O. and Fan, Z. (2012). *ChemPhysChem* 13: 2551–2560.

117 Jain, P.K. and El-Sayed, M.A. (2010). *Chem. Phys. Lett.* 487: 153–164.

118 Sherry, L.J., Chang, S.-H., Schatz, G.C. et al. (2005). *Nano Lett.* 5: 2034–2038.

119 Agrawal, A., Kriegel, I., and Milliron, D.J. (2015). *J. Phys. Chem. C* 119: 6227–6238.

120 Goris, B., Guzzinati, G., Fernández-López, C. et al. (2014). *J. Phys. Chem. C* 118: 15356–15362.

121 Tsoulos, T.V., Atta, S., Lagos, M.J. et al. (2019). *Nanoscale* 11: 18662–18671.

122 Sousa-Castillo, A., Comesaña-Hermo, M., Rodríguez-González, B. et al. (2016). *J. Phys. Chem. C* 120: 11690–11699.

123 Nien, L.-W., Lin, S.-C., Chao, B.-K. et al. (2013). *J. Phys. Chem. C* 117: 25004–25011.

124 Anger, P., Bharadwaj, P., and Novotny, L. (2006). *Phys. Rev. Lett.* 96: 113002.

125 Carminati, R., Greffet, J.-J., Henkel, C., and Vigoureux, J.M. (2006). *Opt. Commun.* 261: 368–375.

126 Govorov, A.O. and Carmeli, I. (2007). *Nano Lett.* 7: 620–625.

127 Khanal, B.P., Pandey, A., Li, L. et al. (2012). *ACS Nano* 6: 3832–3840.

128 Naiki, H., Masuhara, A., Masuo, S. et al. (2013). *J. Phys. Chem. C* 117: 2455–2459.

129 Swearer, D.F., Zhao, H., Zhou, L. et al. (2016). *Proc. Natl. Acad. Sci.* 113: 8916–8920.

130 Spata, V.A. and Carter, E.A. (2018). *ACS Nano* 12: 3512–3522.

131 Li, H., Wu, H., Zhai, Y. et al. (2013). *ACS Catal.* 3: 2045–2051.

132 Li, Z. and Kurouski, D. (2020). *J. Phys. Chem. C* 124: 12850–12854.

133 Li, Z., Wang, R., and Kurouski, D. (2020). *J. Phys. Chem. Lett.* 11: 5531–5537.

134 Jackson, J.D. (2007). *Classical Electrodynamics*. Wiley.

135 Pelton, M. and Bryant, G.W. (2013). *Introduction to Metal-Nanoparticle Plasmonics*. Hoboken, NJ: Wiley; Science Wise Publishing.

136 Bohren, C.F. and Huffman, D.R. (1998). *Absorption and Scattering of Light by Small Particles*. Wiley-VCH Verlag GmbH: Weinheim, Germany.

137 Wang, H., Fu, K., Drezek, R.A., and Halas, N.J. (2006). *Appl. Phys. B* 84: 191–195.

138 Atwater, H.A. and Polman, A. (2010). *Nat. Mater.* 9: 205–213.

139 Catchpole, K.R. and Polman, A. (2008). *Appl. Phys. Lett.* 93: 191113.

140 Zhang, X., Li, X., Reish, M.E. et al. (2018). *Nano Lett.* 18: 1714–1723.

141 Li, X., Zhang, X., Everitt, H.O., and Liu, J. (2019). *Nano Lett.* 19: 1706–1711.

142 Govorov, A.O. and Richardson, H.H. (2007). *Nano Today* 2: 30–38.

143 Palermo, G., Cataldi, U., Condello, A. et al. (2018). *Nanoscale* 10: 16556–16561.

144 Keblinski, P., Cahill, D.G., Bodapati, A. et al. (2006). *J. Appl. Phys.* 100: 054305.

145 Mazzanti, A., Yang, Z., Silva, M.G. et al. (2019). *Proc. Natl. Acad. Sci.* 116: 8161–8166.

146 Baffou, G. and Quidant, R. (2013). *Laser Photonics Rev.* 7: 171–187.

147 Yu, P., Besteiro, L.V., Huang, Y. et al. (2019). *Adv. Opt. Mater.* 7: 1800995.

148 Mubeen, S., Lee, J., Singh, N. et al. (2013). *Nat. Nanotechnol.* 8: 247–251.
149 Zhang, X., Kumari, G., Heo, J., and Jain, P.K. (2018). *Nat. Commun.* 9: 3056.
150 Zhang, X., Li, X., Zhang, D. et al. (2017). *Nat. Commun.* 8: 14542.
151 Khorashad, L.K., Besteiro, L.V., Correa-Duarte, M.A. et al. (2020). *J. Am. Chem. Soc.* 142: 4193–4205.
152 Zhang, Q., Thrithamarassery Gangadharan, D., Liu, Y. et al. (2016). *J. Materiomics* 3: 33–50.
153 Yu, S., Wilson, A.J., Kumari, G. et al. (2017). *ACS Energy Lett.* 2: 2058–2070.
154 Kumaravel, V., Bartlett, J., and Pillai, S.C. (2020). *ACS Energy Lett.* 5: 486–519.
155 Thangamuthu, M., Santschi, C., and Martin, O.J.F. (2019). *Faraday Discuss.* 214: 399–415.
156 Christopher, P., Xin, H., and Linic, S. (2011). *Nat. Chem.* 3: 467–472.
157 Kochuveedu, S.T., Jang, Y.H., and Kim, D.H. (2013). *Chem. Soc. Rev.* 42: 8467.
158 Guo, S., Li, J., Dong, S., and Wang, E. (2010). *J. Phys. Chem. C* 114: 15337–15342.
159 Bera, S., Lee, J.E., Rawal, S.B., and Lee, W.I. (2016). *Appl. Catal. Environ.* 199: 55–63.
160 Wen, M., Mori, K., Kuwahara, Y., and Yamashita, H. (2017). *ACS Energy Lett.* 2: 1–7.
161 Verma, P., Kuwahara, Y., Mori, K., and Yamashita, H. (2015). *J. Mater. Chem. A* 3: 18889–18897.
162 Qin, J. and Zeng, H. (2017). *Appl. Catal. Environ.* 209: 161–173.
163 Rajender, G., Choudhury, B., and Giri, P.K. (2017). *Nanotechnology* 28: 395703.
164 Cai, G., Yu, Z., Ren, R., and Tang, D. (2018). *ACS Sens.* 3: 632–639.
165 Xu, Y., Xu, H., Yan, J. et al. (2013). *Phys. Chem. Chem. Phys.* 15: 5821.
166 Hung, K.-C., Lai, Y.-H., and Lin, T.-W. (2016). *Cat. Sci. Technol.* 6: 4020–4026.
167 Özbek, M.O. and van Santen, R.A. (2013). *Catal. Lett.* 143: 131–141.
168 Park, D. (1987). *J. Catal.* 105: 81–94.
169 Zhang, X., Ke, X., and Yao, J. (2018). *J. Mater. Chem. A* 6: 1941–1966.
170 Yu, S., Wilson, A.J., Heo, J., and Jain, P.K. (2018). *Nano Lett.* 18: 2189–2194.
171 Hentschel, M., Schäferling, M., Weiss, T. et al. (2012). *Nano Lett.* 12: 2542–2547.
172 Fan, Z. and Govorov, A.O. (2012). *Nano Lett.* 12: 3283–3289.
173 Wang, Z., Cheng, F., Winsor, T., and Liu, Y. (2016). *Nanotechnology* 27: 412001.
174 Hentschel, M., Schäferling, M., Duan, X. et al. (2017). *Sci. Adv.* 3: e1602735.
175 Wang, W., Besteiro, L.V., Liu, T. et al. (2019). *ACS Photonics* 6: 3241–3252.
176 Fan, Z. and Govorov, A.O. (2010). *Nano Lett.* 10: 2580–2587.
177 Kuzyk, A., Schreiber, R., Fan, Z. et al. (2012). *Nature* 483: 311–314.
178 Liu, T., Besteiro, L.V., Liedl, T. et al. (2019). *Nano Lett.* 19: 1395–1407.
179 Shen, X., Zhan, P., Kuzyk, A. et al. (2014). *Nanoscale* 6: 2077.
180 Saito, K. and Tatsuma, T. (2018). *Nano Lett.* 18: 3209–3212.